Journal of Structural Geology 134 (2020) 103980

Contents lists available at ScienceDirect

Journal of Structural Geology

journal homepage: http://www.elsevier.com/locate/jsg

The effects of quartz Dauphiné twinning on strain localization in a mid-crustal shear zone

Courtney McGinn [a,1], Elena A. Miranda [a,*], Lonnie J. Hufford [b,c]

[a] Department of Geological Sciences, California State University-Northridge, 18111 Nordhoff St, Northridge, CA, 91330, USA
[b] Scripps Institution of Oceanography, University of California San Diego, 8622 Kennel Way, La Jolla, CA, 92037, USA
[c] Structural Geology and Tectonics Group, Geological Institute, Department of Earth Sciences, ETH Zurich, Sonneggstrasse 5, 8092, Zurich, Switzerland

ARTICLE INFO

Keywords:
Dauphiné twins
Quartz
EBSD
Grain boundary migration
Microstructure
Transpression
Fiordland

ABSTRACT

We use microstructural, electron backscatter diffraction (EBSD), and crystal vorticity axis (CVA) analyses to evaluate the effects of quartz Dauphiné twinning on strain localization. We compare a granodiorite mylonite and a tonalite mylonite from the Grebe Shear Zone, a mid-crustal transpressional shear zone in Fiordland, New Zealand. EBSD analysis reveals identical quartz grain boundary migration dynamic recrystallization microstructures in both samples, with abundant Dauphiné twinning only in the granodiorite mylonite. Bulk CVA patterns further distinguish the untwinned and Dauphiné-twinned samples, indicating a transition from simple shear-to pure shear-dominated transpression, respectively. The quartz CVA pattern from the Dauphiné-twinned sample indicates that twinned and untwinned grains record a transition from simple shear-to pure shear-dominated deformation, respectively. Pole figures of the Dauphiné-twinned sample reveal high-temperature slip systems in the untwinned and Dauphiné-twinned grains. We conclude that Dauphiné twinning formed early in transpression, and rendered the twinned grains less deformable relative to the untwinned grains over time. The effectiveness of Dauphiné twinning in localizing strain is therefore strongly influenced by its timing relative to the evolving shear zone kinematic deformation geometry.

1. Introduction

High temperature quartz deformation is rarely preserved in naturally deformed rocks (e.g. Stipp et al., 2002), though many experimental studies exist on this topic (Cross et al., 2017; Hirth and Tullis, 1992; Mainprice et al., 1986; Minor et al., 2018; Morales et al., 2011; Stipp et al., 2010; Stipp and Tullis, 2003). In addition, few studies exist that investigate how Dauphiné twins affect dynamic recrystallization (DRX) at high temperatures (>600 °C) (Mainprice et al., 1986; Pehl and Wenk, 2005; Piazolo et al., 2005; Tullis et al., 1973; Tullis and Tullis, 1972). The study of Dauphiné twinning is important because of the potential for Dauphiné twinning to be used as a paleostress indicator, especially given the difficulty in applying grain size piezometry to grain boundary migration (GBM) DRX microstructures. Dauphiné twinning, described as a 180° rotation about the *c*-axis (Rahl et al., 2018; Thomas and Wooster, 1951; Tullis and Tullis, 1972), allows the positive and negative rhombs and <*a*> directions to be exchanged without changing [*c*] (Rahl et al., 2018; Thomas and Wooster, 1951; Tullis and Tullis, 1972). Natural and experimental studies both conclude that Dauphiné twinning allows large strains to be accommodated due to the twins' ability to switch between the positive and negative <*a*> directions (Lloyd, 2004; Menegon et al., 2011; Morales et al., 2014; Pehl and Wenk, 2005; Wenk et al., 2007, 2006). Furthermore, quartz has anisotropic elastic properties resulting in the pole to the *z*-plane being twice as stiff as the pole to *r*-plane (Rahl et al., 2018; Wenk et al., 2009). This results in a competence contrast between the more deformable *r*-twin and less deformable *z*-twin, with the *r*-twin bands being the preferred site for dynamic recrystallization (Menegon et al., 2011). Studies of naturally deformed rocks have mainly focused on Dauphiné twinning in rocks that underwent subgrain rotation (SGR) dynamic recrystallization (Lloyd, 2004; Menegon et al., 2011; Morales et al., 2011). The interaction between Dauphiné twins and grain boundary migration (GBM) in quartz is an under-studied process in naturally deformed rocks (Neumann, 2000; Piazolo et al., 2005) that is likely to play a significant role in how strain localizes and is maintained in middle and lower crustal shear zones.

In this study, we investigate the role of Dauphiné twins in strain

* Corresponding author.
E-mail address: elena.miranda@csun.edu (E.A. Miranda).
[1] Present address: Diavik Diamond Mine, Rio Tinto, #300 Northwest Tower 5201 50th Ave., Yellowknife, NT X1A2P8 Canada.

https://doi.org/10.1016/j.jsg.2020.103980
Received 11 October 2018; Received in revised form 10 December 2019; Accepted 6 January 2020
Available online 14 February 2020

localization processes at high temperatures (>600 °C) where quartz microstructures are consistent with GBM DRX. We build on the work of Menegon et al. (2011) by analyzing samples that have deformed via GBM rather than SGR, and we build on the work of Neumann (2000) and Piazolo et al. (2005) by further exploring the migration of twins and their effect on rock microstructure. Fiordland, New Zealand, provides an ideal location to investigate such deformation due to a network of exhumed shear zones that expose middle and lower crust (Allibone et al., 2009a; Klepeis et al., 2004; Marcotte et al., 2005; Schwartz et al., 2017; Scott, 2013; Scott et al., 2011). These zones provide the opportunity to analyze how deformation processes vary with crustal depth. We specifically focus on middle crust samples from the northern, along-strike extension of the Grebe Shear Zone (Allibone et al., 2009b), a mid-crustal shear zone in this network (Schwartz et al., 2017; Scott et al., 2009a,b, 2011; Scott, 2013).

We analyze two representative mylonites, a tonalite mylonite and a granodiorite mylonite, which differ primarily by composition, but also in the intensity of quartz Dauphiné twin development. The granodiorite mylonite has prevalent Dauphiné twinning while the quartz in the tonalite mylonite is nearly untwinned. These two samples provide a comparison of the role that Dauphiné twinning plays in strain localization. We show that Dauphiné twinning initially accommodated strain, but these grains became less deformable over time as GBM promoted growth of other grains more favorably oriented for deformation relative to the Dauphiné-twinned grains.

2. Geologic background

During the Early Cretaceous, New Zealand was part of the convergent boundary along eastern Gondwanaland, and subduction produced a narrow belt of magmatism forming the Median Batholith (Mortimer et al., 1999). The median batholith was built in two installments, forming the inboard and outboard arc rocks (Allibone et al., 2009a; Schwartz et al., 2017). Crustal-scale shear zones developed near the boundary between the outboard (Carboniferous-Early Cretaceous) and inboard (Early to Late Cretaceous) Median Batholith (Scott et al., 2011). This boundary is largely marked by the Indecision Creek Shear Zone in the lower crust (Klepeis et al., 2004; Marcotte et al., 2005) and the Grebe Shear Zone (GSZ) in the middle crust. The GSZ was active from 129 to 116 Ma (Buriticá et al., 2019; Scott et al., 2011) during a period of contraction and transpression (Marcotte et al., 2005; Allibone and Tulloch, 2008; Scott et al., 2011; Klepeis et al., 2016), where the rocks were deformed under amphibolite conditions. The GSZ is mostly developed within Darran Suite rocks (230-136 Ma), which includes the Hunter and

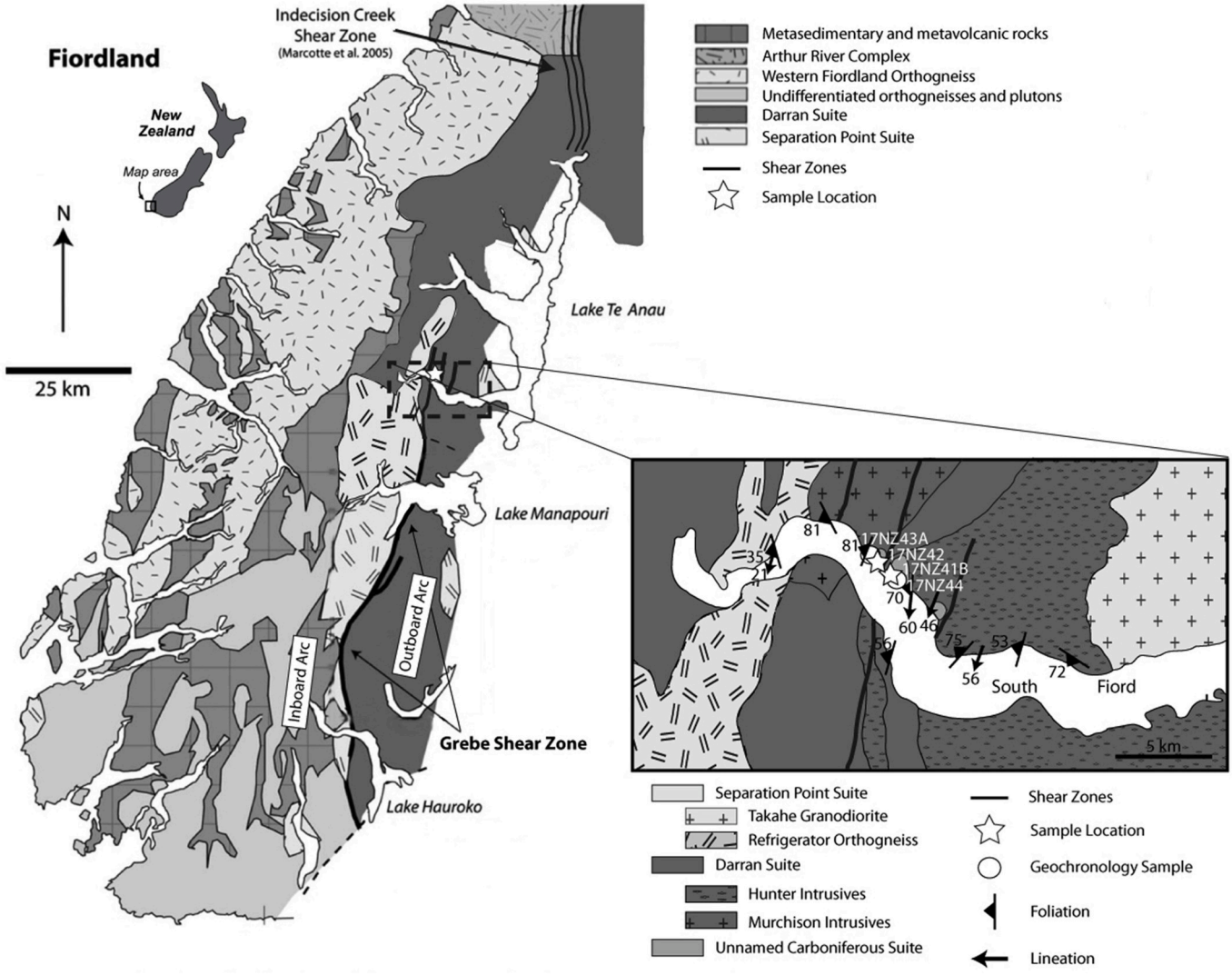

Fig. 1. Simplified geologic map of Fiordland, New Zealand, modified after Scott et al. (2011), Rattenbury and Isaac (2012), Klepeis et al. (2016), and Buriticá et al. (2019). The dashed box encloses the field area for this study. The white stars indicate the location of samples used in this study, and the white circles indicate geochronology samples used to constrain the age of fabric development in the northern extension of the Grebe Shear Zone (Buriticá et al., 2019).

Murchison Intrusives (Allibone et al., 2009a; Scott et al., 2011), and it is also developed in small Carboniferous-aged plutons found within the Darran Suite (Rattenbury and Isaac, 2012). The Darran Suite and Carboniferous plutons are compositionally and texturally heterogeneous, ranging from gabbro to granite and undeformed to foliated, respectively (Allibone et al., 2009a).

The samples used in this study were collected along the north shore of South Fiord in Lake Te Anau, within a mid-crustal shear zone that is the along-strike northern extension of the GSZ (Allibone et al., 2009b) (Fig. 1). The distributed shear zone (~5 km) separates the Hunter and Murchison Intrusives, and contains laterally continuous (3–15 m), high-strain zones that grade from mylonite to ultramylonite. The Lake Te Anau mylonites formed in response to Cretaceous transpression (125-116 Ma) along the GSZ, with Zr-in-titanite temperatures from six samples indicating deformation temperatures of 610–660 °C (Buriticá et al., 2019). Pressure estimates are not available for the Te Anau mylonites, but average pressures for Darran Suite rocks exposed ~20 km south of the Te Anau mylonites range from ~5 to 6 kbar (Scott et al., 2009a,b), corresponding to the middle crust. The Te Anau mylonitic foliations primarily strike SW and dip moderately to steeply NW, with lineations plunging shallowly to moderately towards the SSW. The lineations steepen from west to east across the shear zone. We have selected two high-strain samples from this shear zone that display differences in the relative amount of Dauphiné twinning, and we target these for microstructural and electron backscatter diffraction (EBSD) analysis. 'insert Fig. 1'.

Our two samples are a garnet-bearing muscovite tonalite mylonite (17NZ41B) and a biotite granodiorite mylonite (17NZ42) within the Te Anau mylonites, which we refer to as the untwinned quartz sample and the Dauphiné-twinned quartz sample, respectively (see Supplemental Fig. SP1 for hand sample photos). S–C fabric development shows predominantly sinistral shear sense indicators in plagioclase porphyroclasts, indicating top-to-the-NE sense of shear. The untwinned sample (tonalite mylonite) is from an unnamed Carboniferous suite of plutons (Buriticá, 2018) (Fig. 1), and has a mylonitic fabric oriented at 185°, 70° NW and a lineation of 19°/186° SW. A nearby sample (17NZ44) with similar mineralogy and microstructures yielded a U–Pb zircon age of 342.8 ± 2.5 Ma (Buriticá et al., 2019). The Dauphiné-twinned sample (granodiorite mylonite), also part of the unnamed Carboniferous suite (Buriticá, 2018), has a mylonitic fabric oriented at 201°, 81° NW; this sample has a U–Pb zircon age of 354.3 ± 7.8 Ma (Ringwood, 2018). A nearby sample (17NZ43A) has a U–Pb zircon age of 344.0 ± 7.6 Ma (Ringwood, 2018), and titanite aligned with the mylonitic fabric of this nearby sample provided a U–Pb age of 123.2 ± 9.6 Ma and a Zr-in-titanite temperature of 608 ± 6 °C (Buriticá et al., 2019), consistent with the timing and temperature conditions of GSZ deformation (Buriticá et al., 2019). Furthermore, these temperatures and the pressure estimates (5–6 kbar) indicate that the quartz deformed within the α-field of quartz. Both samples were cut perpendicular to the foliation and parallel to the lineation for microstructural and EBSD analysis.

3. Methods

3.1. Light microscopy

The mineral phases and deformation microstructures were identified using a Nikon Eclipse 50iPol polarizing microscope and a Leica MZ8 macroscope. After a thorough analysis of each sample utilizing plane and cross-polarized light, locations were selected for further microstructural analysis via EBSD.

3.2. EBSD

EBSD data were collected at University of California San Diego using a ThermoFisher Apreo S LoVac scanning electron microscope (SEM) equipped with an Oxford Instruments Symmetry EBSD detector and AZtec EBSD acquisition software. Ultra-polished samples were analyzed under low vacuum conditions. Beam maps were generated to characterize the deformation microstructures and determine the crystallographic orientation of grains. For this study, we constructed an EBSD map from each sample (the untwinned quartz and Dauphiné-twinned quartz samples), focusing on the recrystallized quartz bands. The working conditions for each map are shown in Table 1. 'insert Table 1'.

We used the MTEX toolbox (v. 5.1.1) for MATLAB to post-process the EBSD data and create maps (Bachmann et al., 2010; Hielscher and Schaeben, 2008). In all maps, we define the grain boundaries as having ≥10° of misorientation, and we specify a minimum number of 10 pixels to define a grain. We identify Dauphiné twins as having a 60° ±1.5° rotation around the *c*-axis (Lloyd, 2004; Menegon et al., 2011; Stipp and Kunze, 2008). We use phase maps to visualize mineral distribution, and inverse pole figure (IPF-Z) maps to show grain orientations relative to the foliation pole. The mis2mean maps calculate the misorientation angle between each pixel in a grain relative to the grain's mean orientation, and we use these maps as a measure of intragrain crystal distortion. The kernel average misorientation maps calculate the average misorientation between each pixel and its nearest neighbors, and we use these maps to visualize the location of low-angle (≤2°) misorientations that contribute to intragrain distortion in the grains.

We used the MTEX software to plot crystallographic preferred orientation (CPO) data and crystallographic vorticity axis (CVA) data. We plot CPO data in lower hemisphere, equal area pole figures, and we contoured the pole figures using an Orientation Distribution Function (ODF) and a half width of 10°. The contour density of crystallographic orientations is indicated by multiples of uniform distribution (m.u.d). We plot the CPO data in either the kinematic reference frame or the vorticity normal reference frame based on the CVA results (Giorgis et al., 2016). We use CVA analysis to interpret the kinematic deformation geometry of the shear zone. CVA analysis uses rotation statistics to calculate the dispersion axes of grains from EBSD-derived crystallographic orientations with the goal of defining an aggregate vorticity axis that places constraints on deformation kinematics that are independent of the foliation and lineation orientation (Michels et al., 2015). We used the open-source CVA analysis code available on GitHub (https://github.com/zmichels/CVA) to construct CVA plots. We completed CVA analysis for both the untwinned and Dauphiné-twinned samples, making plots for the bulk sample (all minerals together) and for the constituent minerals (biotite, muscovite, plagioclase and quartz), and we display the CVA data in lower hemisphere, equal-area projections.

4. Results

4.1. Untwinned quartz sample (17NZ41B) microstructures

4.1.1. Microstructures from light microscopy

Light microscopy reveals the development of deformation microstructures in plagioclase and quartz. Fine-grained plagioclase (45%) and coarser-grained quartz (35%) are separated into bands (Fig. 2a) within an S–C mylonite (Supplemental Fig. SP2) where the muscovite that has minor alteration to chlorite is associated with the C-shears, and the slightly coarser quartz grains are associated with domains exhibiting the S-fabric. Muscovite and chlorite form anastomosing bands, separating the plagioclase and quartz bands, containing grains at variable orientations to foliation (Fig. 2b). Fine-grained plagioclase (average grain diameter <20 μm) has bulging grain boundaries that are pinned by muscovite grains (Fig. 2c). Rare plagioclase porphyroclasts are fairly altered to sericite (Fig. 2d), but are shown to exhibit undulose extinction and local subgrain development, with fine-grained plagioclase present along rims. Quartz bands are nearly monomineralic and composed of completely recrystallized grains that range from fine to coarse-grained (6–700 μm, ~115 μm average). Quartz grains exhibit GBM recrystallization microstructures including undulose extinction and limited subgrain development, and have grain boundaries that range in shape from

Table 1
SEM working conditions used for EBSD data collection.

Sample	Sample Type	Step Size (μm)	Accelerating Voltage (kV)	Emission Current (μA)	Working Distance (mm)	Raw Indexing Rates of EBSD map (%)
Untwinned Quartz Sample (17NZ41B)	tonalite mylonite	2.50	20	84.52	28.8	91.3
Dauphiné-twinned Quartz Sample (17NZ42)	granodiorite mylonite	3.70	20	75.17	27.83	93.4

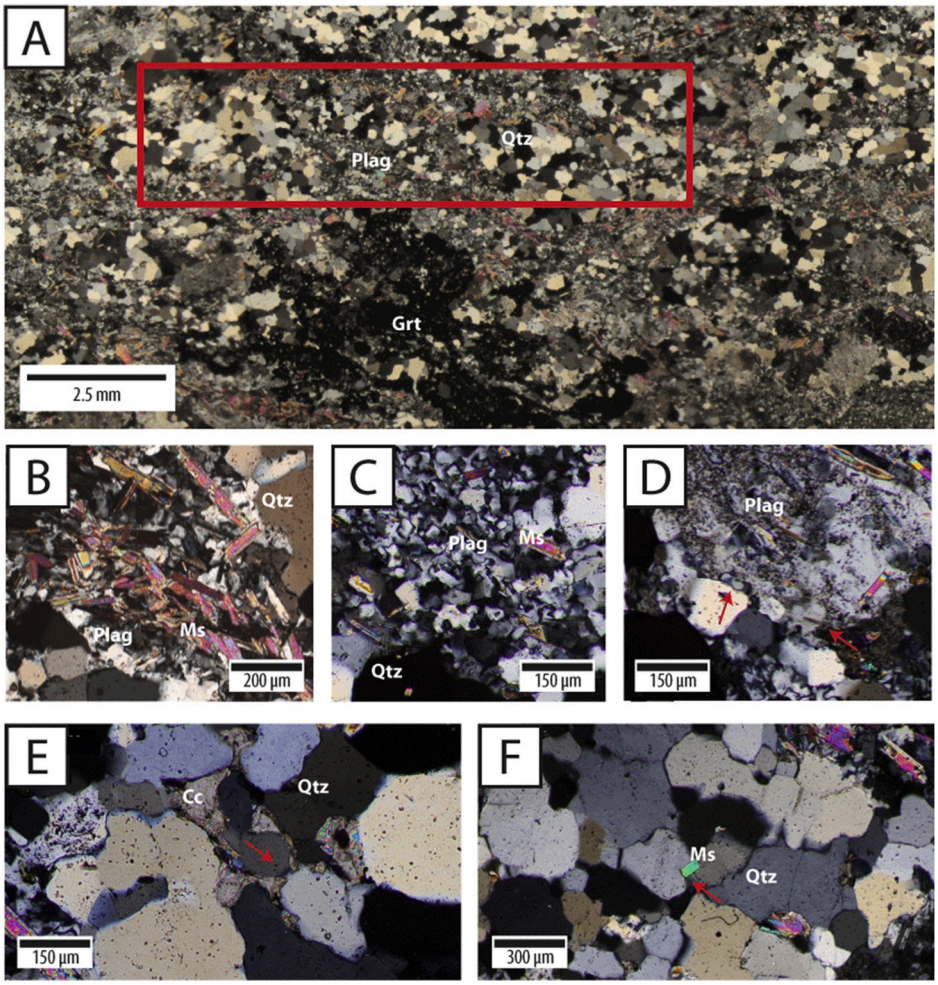

Fig. 2. Photomicrographs of the untwinned quartz sample in cross-polarized light. a) Characteristic banding of quartz and plagioclase with the location of the EBSD map outlined in red. b) Muscovite in variable orientations separating plagioclase and quartz. c) Recrystallized plagioclase pinned by muscovite. d) Altered plagioclase porphyroclast with subgrains (red arrows). e) Quartz grains pinned by calcite (red arrow). f) Quartz grains pinned by muscovite (red arrow). Qtz = quartz, Plag = plagioclase, Grt = Garnet, Ms = Muscovite Cc = Calcite. (For interpretation of the references to color in this figure legend, the reader is referred to the Web version of this article.)

lobate to straight. Quartz grain boundaries are pinned by minor inclusions of both calcite (Fig. 2e) and muscovite grains (Fig. 2f). A quartz-rich band within this S–C mylonite sample was selected for detailed EBSD analysis (Fig. 2a). 'insert Fig. 2'.

4.1.2. *EBSD data from the untwinned quartz sample*

EBSD maps confirm the presence of dynamic recrystallization microstructures in plagioclase and quartz (Fig. 3). The phase map shows that the plagioclase domains are closely associated with muscovite (Fig. 3a). Plagioclase, calcite, and muscovite form pinning microstructures in quartz. In plagioclase, the bulging grain boundaries of larger grains and the small, equant recrystallized grains along their grain boundaries indicates BLG recrystallization (Fig. 3b). The quartz IPF-Z orientation map confirms the presence of GBM DRX microstructures observed with light microscopy, and reveals the presence of minor Dauphiné twinning (Fig. 3c). Though there is no overall dominant orientation of quartz grains, there are clusters of similarly-oriented grains separated by a few interstitial grains of different orientations termed 'island grains' in Stipp et al. (2002) (Fig. 3c). Rare subgrains are most common within the coarser, lobate-shaped grains (Fig. 3c). The IPF-Z map shows that the Dauphiné-twinned grains have twins that range in color from brownish-purple to cream, indicating that the twinned grains are oriented with either an *r*-pole or *z*-pole parallel to the foliation normal. The quartz mis2mean map (Fig. 3d) reveals an overall low amount of intra-grain crystal plasticity in the grains, though intra-grain variations in mis2mean values define the locations of subgrains within coarser grains. The KAM map shows many grains with fewer low-angle misorientations forming convex lobes into grains with higher density of misorientations (Fig. 3e). 'insert Fig. 3'.

4.2. *Dauphiné-twinned quartz sample (17NZ42) microstructures*

4.2.1. *Microstructures from light microscopy*

Light microscopy analysis of plagioclase and quartz shows extensive recrystallization of both minerals. The quartz (35%) and plagioclase (50%) bands (Fig. 4a) are separated by bands of biotite and minor

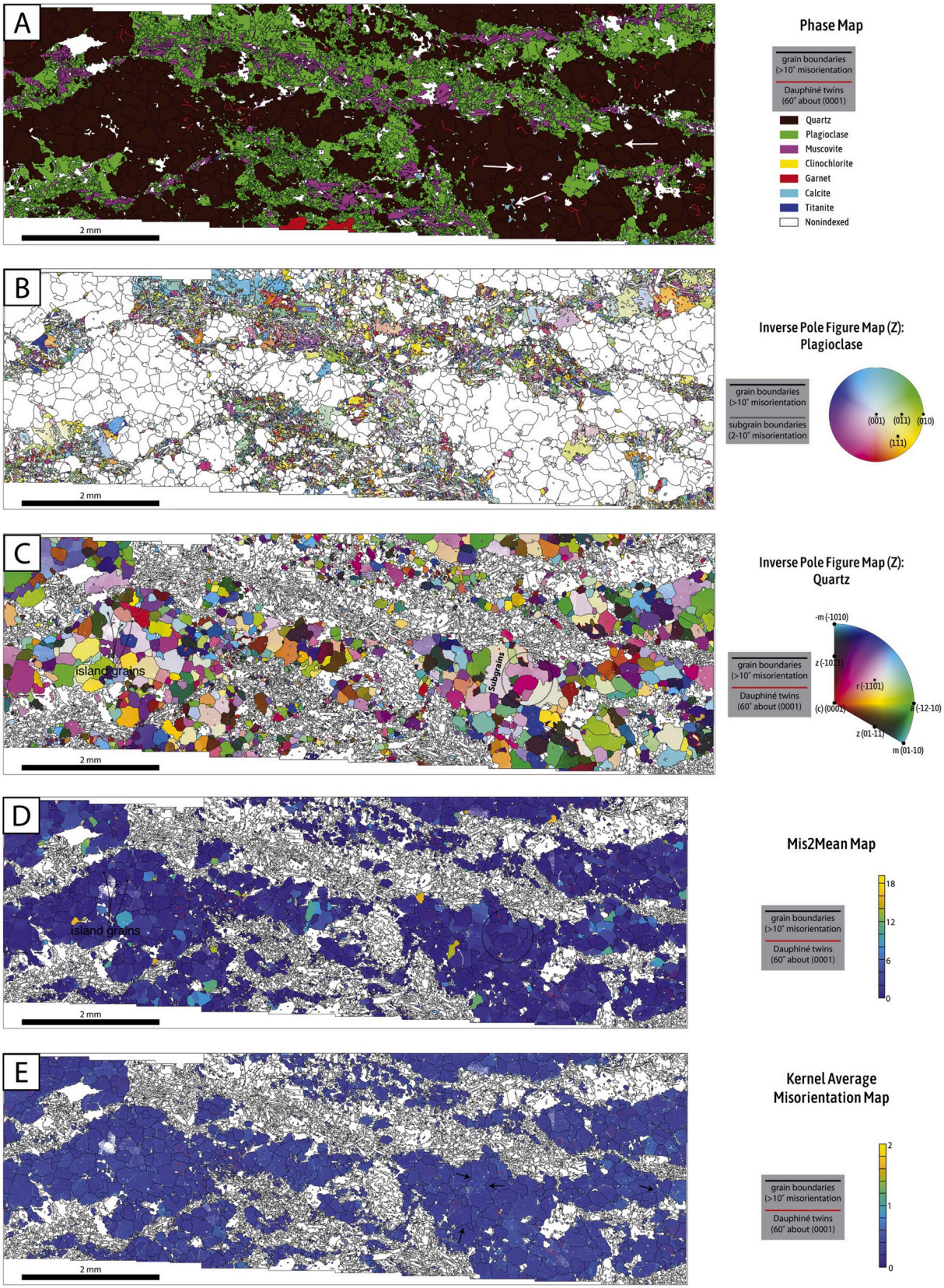

(caption on next page)

Fig. 3. EBSD maps of quartz and plagioclase bands in the untwinned quartz sample. a) White arrows in the phase map highlight pinning microstructures in quartz due to minor calcite, plagioclase, and muscovite. b) The plagioclase IPF-Z map shows larger grains with bulging grain boundaries surrounded by smaller, equant grains. c) The quartz IPF-Z map highlights the presence of minor Dauphiné twinning and rare subgrains. Examples of island grains are shown with black arrows. The encircled area shows cross-cutting relationships between a grain with lots of subgrains (light pink) and a grain without subgrains (dark pink) that cuts it; these grains are also referred to in Fig. 8 d) The mis2mean map shows overall low intra-grain crystal plasticity, and the grains with a relatively higher mis2mean value (black arrows) contain subgrains. The island grains (black arrows) have low values of intragrain misorientation. The encircled area shows cross-cutting relationships between a grain with higher amounts of intragrain misorientation cut by a grain with lower intragrain misorientation. The white arrows show contrasts in intragrain misorientation across twin boundaries. e) the kernel average misorientation map reveals grains with fewer low-angle misorientations forming convex lobes into grains with a higher density of misorientations indicated by black arrows. (For interpretation of the references to color in this figure legend, the reader is referred to the Web version of this article.)

muscovite (15%) that contain grains oriented parallel and oblique to foliation (Fig. 4b). The quartz domains align with the S-shears and the biotite and muscovite domains align with the C-shears in the fabric (Supplemental Fig. SP3). Plagioclase is fine-grained (~50 μm average diameter), and within the plagioclase-rich domains, the fine grains are pinned by interstitial quartz and biotite (Fig. 4c). Plagioclase porphyroclasts are not common (see supplemental Fig. SP3), but porphyroclast-shaped domains of recrystallized plagioclase both with relict porphyroclast cores and without relict cores (Fig. 4d) are present. In contrast, the recrystallized quartz is fairly coarse-grained compared to plagioclase, but with highly variable grain sizes (9–1000 μm, ~230 μm average). The quartz grains commonly show distinctive microstructures

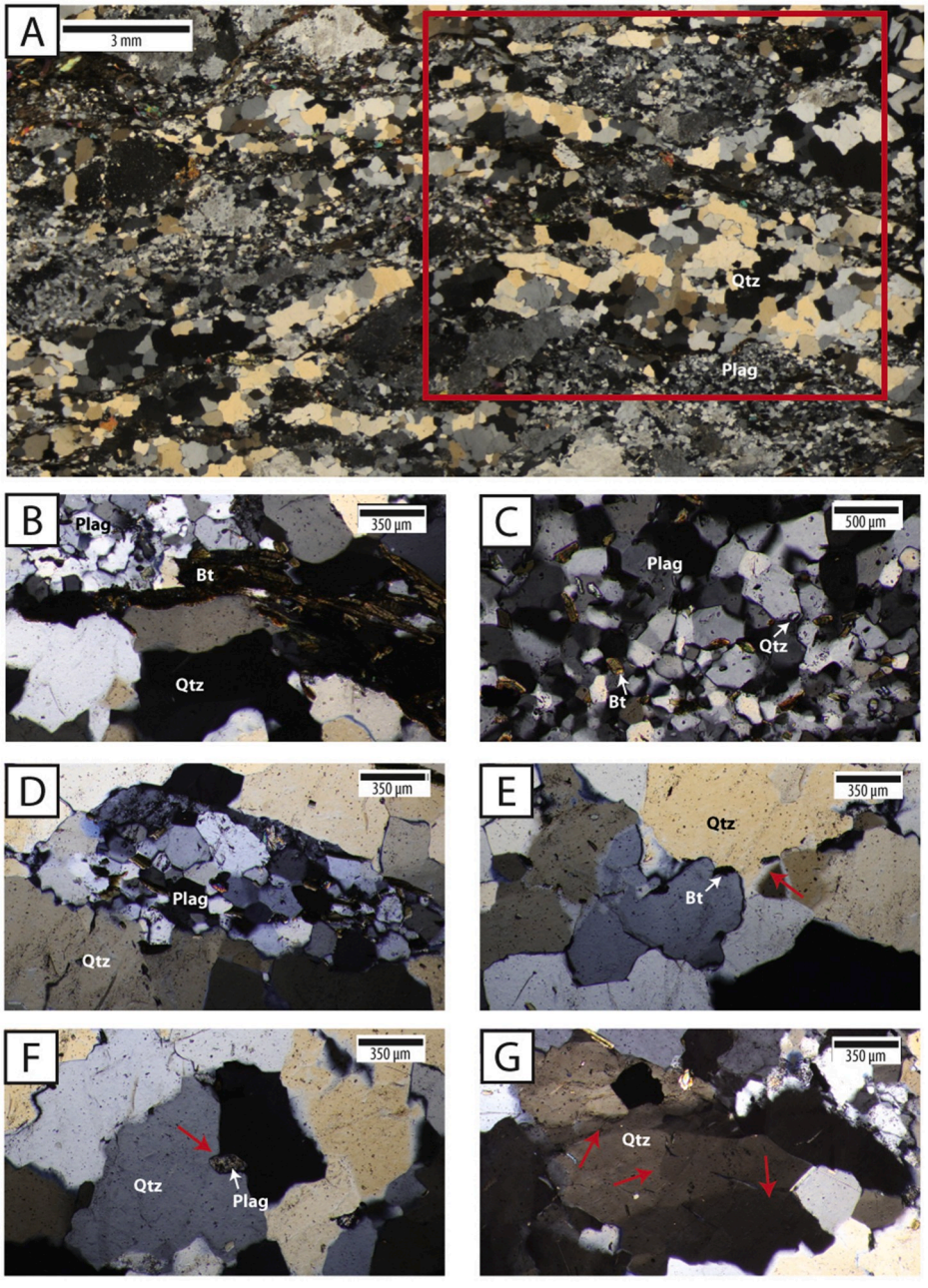

Fig. 4. Photomicrographs of the Dauphiné-twinned sample in cross-polarized light. a) Characteristic fabric with coarse-grained quartz and fine-grained plagioclase forming compositional bands. The red box indicates the area of EBSD analysis. b) Biotite with variable orientations at the interface between quartz- and plagioclase-rich bands. c) Fine-grained, recrystallized plagioclase pinned by muscovite and quartz. d) Porphyroclast-shaped region of recrystallized plagioclase grains that show undulose extinction and subgrain development. e) Quartz pinned by biotite (red arrow). f) Quartz pinned by altered plagioclase (red arrow). g) Quartz grain showing chessboard extinction and the development of subgrains (red arrows). Qtz = Quartz, Plag = Plagioclase, Bt = Biotite. (For interpretation of the references to color in this figure legend, the reader is referred to the Web version of this article.)

of GBM recrystallization, including interpenetrating lobate grain boundaries, undulose extinction, some subgrain development, and grain boundary pinning by biotite (Fig. 4e), muscovite, and plagioclase (Fig. 4f). In addition, chessboard extinction patterns are observed (Fig. 4g). Domains of recrystallized quartz grains exhibiting these distinctive microstructures were targeted for EBSD analysis (Fig. 4a). 'insert Fig. 4'.

4.2.2. EBSD data from the Dauphiné-twinned quartz sample

EBSD maps confirm the presence of dynamic recrystallization microstructures in plagioclase and quartz (Fig. 5). The phase map reveals alternating domains of recrystallized plagioclase and quartz, where the grain size of quartz is generally larger than that of plagioclase. (Fig. 5a). Micas are associated with the plagioclase domains, with most grains oriented parallel to foliation, and a small proportion oriented oblique or at high angles to foliation. The plagioclase IPF-Z map shows host-control relationships between relict and commonly twinned porphyroclast cores and their surrounding elongate-to equant-shaped recrystallized grains, consistent with microstructures produced by subgrain rotation recrystallization (SGR) (Fig. 5b). The quartz IPF-Z map confirms the presence of the optically observed GBM microstructures and reveals the presence of prevalent Dauphiné twinning. The IPF-Z map reveals 'island grains' (stars in Fig. 5c), but no dominant color suggesting a preferred orientation of quartz grains. However, the Dauphiné twins tend to be oriented obliquely or normal to the foliation. Grains with minor or absent twinning have convex lobes that protrude into the Dauphiné-twinned grains. The mis2mean map demonstrates that quartz has an overall low amount of intra-grain crystal plasticity, particularly in smaller grains (20–130 μm in diameter) that have minor or absent twinning (Fig. 5d). The KAM map shows that grains with fewer lower angle boundaries have convex grain boundaries that protrude into grains with prevalent twinning, and into other grains having a greater density of low-angle boundaries. 'insert Fig. 5'.

4.3. Crystallographic vorticity axis analysis

Crystallographic vorticity axis (CVA) analysis for the untwinned quartz sample reveals distinct differences in the CVA geometry for the bulk sample and the individual minerals. For the untwinned quartz sample, the dispersion axes for the bulk sample (Fig. 6a) show a Y-axis maximum within a girdle along the Y-Z plane. The muscovite CVA plot (Fig. 6b) shows two maxima: a Y-axis maximum and a wide X-axis maximum. The quartz CVA plot (Fig. 6c) shows a Y-axis maximum within a girdle extending along the X–Y plane. The plagioclase CVA plot is most similar to the bulk CVA pattern, with a Y-axis maximum within a girdle along the Y-Z plane (Fig. 6d). 'insert Fig. 6'.

CVA analysis for the Dauphiné-twinned quartz sample also shows differences in the CVA geometry for the bulk sample and the individual minerals, but the CVA geometry is also different compared to the untwinned quartz sample. The CVA bulk data plot shows a girdle of vorticity axes oriented oblique to the X–Y plane, with a broad maximum centered in the top right quadrant and extending towards the Y-axis (Fig. 6e). The biotite CVA plot (Fig. 6f) shows a girdle slightly oblique to the X–Y plane that contains a strong X-axis maximum on the primitive. The quartz CVA plot (Fig. 6g) is similar to the bulk CVA pattern in that there is a girdle of vorticity axes oriented oblique to the X–Y plane with a maximum in the top right quadrant, but the quartz pattern shows a higher density of axes within the girdle relative to the bulk pattern. The CVA pattern of the twinned quartz grains (Fig. 6h) shows an elongate maximum extending from the Y-axis to the upper right quadrant of the plot where it intersects a weak partial girdle oriented oblique to the X–Y plane. The CVA pattern of the untwinned quartz grains (Fig. 6i) shows a girdle oriented oblique to the X–Y plane, and it is much better developed relative to the CVA pattern of the twinned quartz grains. Within the girdle, there are 3 elongate maxima; the strongest one is centered in the top right quadrant near the Y-Z plane, and the two others lie 30-40° on either side of it. The plagioclase CVA pattern (Fig. 6j) shows a girdle oriented ~30° clockwise relative to the Y-Z plane, with an elongate maxima within it that extends from the Y-axis up towards the top right quadrant.

4.4. Quartz crystallographic orientation data

Pole figure plots for the untwinned quartz sample show a moderate crystallographic preferred orientation (CPO) in quartz that is best expressed in the *c*-axis and positive rhomb *r* {-1101} plots (Fig. 7a). The *c*-axis plot shows a partial girdle oriented ~60° counterclockwise from the Z-axis, and it contains a strong maximum between the Y and Z axes. The *a*-axis {-1-120} plot shows an irregular distribution of *a*-axis orientations and three maxima; in the upper hemisphere plot, there is a maximum parallel to the X-axis, and another in the upper left quadrant. In the lower hemisphere plot, there is a stronger maximum in the bottom left quadrant. The positive rhomb *r* {-1101} plot shows strong alignment of poles to {*r*} parallel to the Z-axis, which is the foliation normal direction. The negative rhomb *z* {01–11} plot shows three weak maxima that are oblique to the X, Y and Z axes. 'insert Fig. 7'.

Pole figure plots for the Dauphiné-twinned sample reveal a CPO in quartz by the presence of a moderately strong fabric that is best expressed in the *c*-axis and negative rhomb *z* {01–11} plots (Fig. 7b). The *c*-axis plot showing all quartz grains has a strong maximum near the primitive, ~30° clockwise from the Z-axis. The *a*-axis {-1-120} plot shows an irregular distribution of *a*-axis orientations. The positive rhomb *r* {-1101} plot shows five weak maxima; none are parallel to the X, Y, and Z axes. The negative rhomb *z* {01–11} plot shows a moderately strong alignment of poles to {*z*} oriented sub-parallel to the X-axis, with a weaker maximum near the Y-axis.

We show pole figures for a subset of twinned quartz grains within the Dauphiné-twinned sample in Fig. 7c (see Supplemental Figure SP5 for map of subset selection). These grains show a CPO in quartz that is best expressed in the *c*-axis and negative rhomb *z* {01–11} plots. The *c*-axis shows a very strong maximum on the primitive, ~20° counterclockwise from the Z-axis. The *a*-axis plot shows two strong maxima in the upper hemisphere, both near the primitive, and oriented ~30° counterclockwise from the X-axis. The lower hemisphere shows a maximum centered near the Y-axis. The positive rhomb *r* {-1101} plot shows three weak maxima with several other subordinate maxima; none are parallel to the X, Y, and Z axes, and there is an absence of fabric parallel to the Z-axis. The negative rhomb *z* {01–11} plot shows a strong alignment of poles to {*z*} oriented 10° clockwise from the X-axis, with two weaker maxima near the Z-axis and the Y-axis.

We show pole figures for a subset of untwinned quartz grains within the Dauphiné-twinned sample in Fig. 7d and e (see Figure Supplemental Fig. SP4 for map of subset selection). Because the twinned and untwinned grains are also distinguished by their distinct patterns in CVA plots (Fig. 6), we display the untwinned grains pole figure plots in different reference frames so that CPO patterns can be interpreted normal to the vorticity axis [i.e., Giorgis et al., 2016]. We plot the untwinned grains pole figures in both the kinematic and the vorticity normal reference frame, the latter of which is decoupled from the kinematic reference frame in pure shear dominated transpression (Fig. 6). In both reference frames, the grains show a CPO that is best expressed in the *c*-axis and negative rhomb *z* {01–11} plots. In the kinematic reference frame (Fig. 7d), the patterns are similar to those of the bulk sample in Fig. 7b. The *c*-axis plot shows a weak cross-girdle fabric, with a maximum in the lower right quadrant, and another offset from the Y-axis. The *a*-axis {-1-120} plot shows three maxima, one along the primitive and ~45° counterclockwise from the Z-axis, and two weaker maxima in the upper right and lower left quadrants. The positive rhomb *r* {-1101} plot shows five weak maxima, with one maximum oriented ~10° counterclockwise from the Z-axis. The negative rhomb *z* {01–11} plot shows a moderately strong alignment of poles to {*z*} oriented sub-parallel to the X-axis, with a weaker maximum in the lower half of

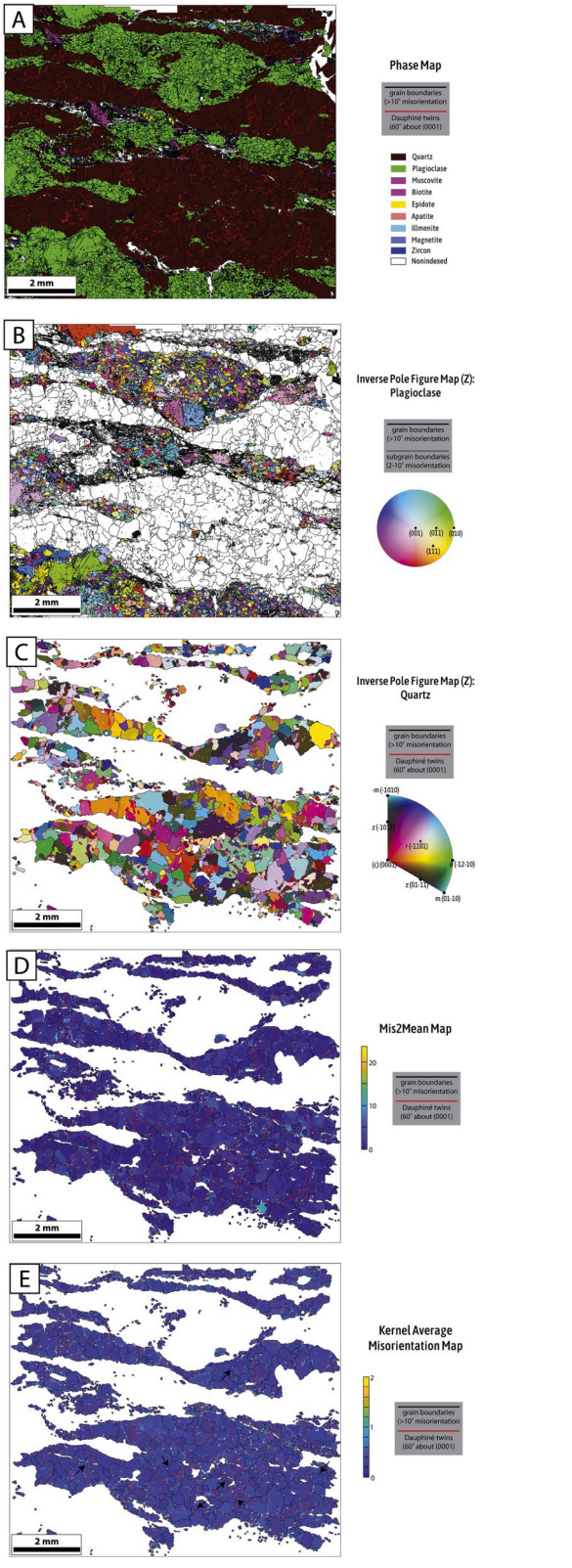

(caption on next column)

Fig. 5. EBSD maps of quartz and plagioclase bands in the Dauphiné-twinned sample. a) Phase map showing abundant quartz and plagioclase, where plagioclase forms relict porphyroclasts. b) IPF-Z map of plagioclase showing host-control relationships between relict porphyroclast cores and the surrounding recrystallized grains. c) IPF-Z map of quartz showing an abundance of Dauphiné twins, the presence of island grains (large twinned grain with white stars at lower right), and rare subgrains that are associated with coarser grains. d) Mis2mean map of quartz showing the overall low intra-grain crystal plasticity of quartz and the contrasts in misorientation across twin boundaries. White arrows indicate parts of twinned grains with lower intragrain misorientation. d) Kernel average misorientation map showing grains with fewer low-angle misorientations forming convex lobes into grains with a higher density of misorientation (indicated by arrows).

the figure, ~45° from the Y-axis and along the Y-Z plane, and a third maximum oriented near the Z-axis. In the vorticity normal reference frame (Fig. 7e), the *c*-axis plot shows a maximum in the lower left quadrant, and another on the primitive, ~15°counterclockwise from the Y-axis. The *a*-axis {-1-120} plot shows one weak maximum in the upper hemisphere and two weak maxima in the lower hemisphere that are aligned along the trace of a plane oriented ~10° counterclockwise from the Z-axis. The positive rhomb *r* {-1101} plot shows a weak and random pattern. The negative rhomb *z* {01–11} plot shows three weak maxima aligned along a trace of a plane oriented ~30° counterclockwise from the Y-axis.

4.5. *Maps of quartz r-pole and z-pole orientation relative to foliation and lineation*

In the untwinned sample, the positive rhomb *r* {-1101} pole figure indicates a preferred orientation of *r*-planes parallel to foliation (Fig. 7a), and the map of quartz grain *r*-pole orientation relative to foliation shows the spatial distribution of those grains (Fig. 8a). In this map, grains having an *r*-pole within 0-10° of the foliation pole are navy blue in color, representing the grains with *r*-planes parallel to foliation. Some navy grains are impinged upon by convex lobes of adjacent grains that have an *r*-pole at high angle to the foliation pole (Fig. 8a). In other locations, 'island grains' (compare Figs. 3c and 8a) with an *r*-pole at high angle to the foliation pole are impinged upon by navy grains. The grains containing twin boundaries are not dominantly navy blue in color; where twin boundaries separate a navy colored part of a grain from a different colored part of a grain, there is not a tendency for the navy side of the twin boundary to form a convex lobe into the adjacent color, either. 'insert Fig. 8'.

In the twinned sample, the negative rhomb *z* {01–11} pole figure indicates a preferred orientation of *z*-planes sub-perpendicular to foliation for the twinned grains population (Fig. 7c), and the map of quartz grain *z*-pole orientation relative to the lineation shows the spatial distribution of these grains (Fig. 8b). In this map, the grains having a *z*-pole within 0-10° of the lineation are navy blue in color, and it is apparent that many of these navy grains are twinned (Fig. 8b). The negative rhomb *z* {01–11} pole figure also shows subordinate maxima near the Z- and Y-axes (Fig. 7c), and we show the spatial distribution of grains that correlate with these subordinate pole figure maxima by showing maps of *z*-pole orientation relative to the foliation pole and *z*-pole orientation relative to the Y-axis in Fig. 8c and d, respectively. In the *z*-pole relative to foliation pole map (Fig. 8c), the majority of navy blue grains are untwinned, and they protrude into and cut across Dauphiné-twinned grains. In the *z*-pole relative to Y-axis map (Fig. 8d), the majority of the navy blue grains are twinned.

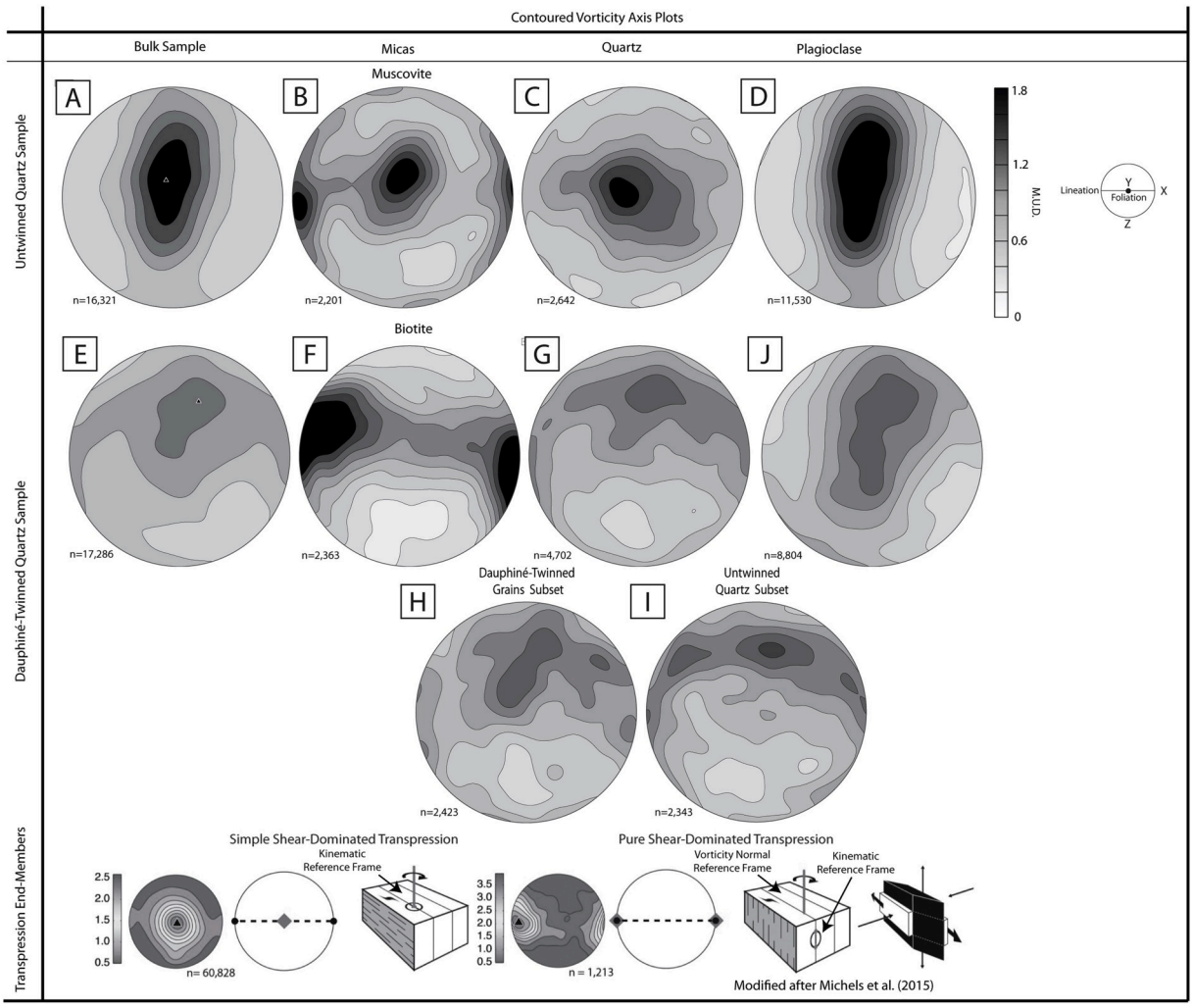

Fig. 6. Crystallographic vorticity axis (CVA) analysis of the untwinned and Dauphiné-twinned quartz samples. Contoured pole figures are equal area, lower hemisphere projections with a 10° contour half width. CVA analysis results for the untwinned quartz sample are displayed for the (a) bulk sample and the individual minerals (b) muscovite (c) quartz and (d) plagioclase. The Dauphiné-twinned quartz sample CVA data are displayed for the (e) bulk sample and the individual minerals (f) biotite (g) quartz (h) subset of Dauphiné-twinned grains (i) subset of untwinned quartz grains, and (j) plagioclase. A key modified after Michels et al. (2015) shows example CVA data for the end members of simple shear-dominated transpression and pure shear-dominated transpression. See Supplemental Figure SP4 for the grains used in the twinned/untwinned quartz subsets of the Dauphiné-twinned quartz sample.

5. Discussion

5.1. Microstructural development and dynamic recrystallization

5.1.1. Untwinned quartz sample

Microstructural observations via light microscopy and EBSD indicate crystal plastic deformation of both quartz and plagioclase, where strain is more prominently partitioned into dynamically recrystallized quartz. Plagioclase is moderately recrystallized based on the presence of finely recrystallized grains along the margins of coarser grains (Fig. 3b), suggesting recrystallization by a BLG recrystallization mechanism. In contrast, quartz displays classic GBM microstructures such as lobate grain shapes (Fig. 3a), grain boundary pinning (Fig. 2e, f, 3a), and 'island' grains (Fig. 3c), all of which indicate highly mobile grain boundaries. The rapid movement of grain boundaries through grain interiors results in recovery and low intra-grain crystal plasticity (Fig. 3d) (e.g., Hirth and Tullis, 1992; Stipp et al., 2002). Efficient dynamic recrystallization of quartz resulted in strain partitioning into the essentially monomineralic S-fabric domains. We interpret the modally abundant quartz as a rheology-controlling, interconnected network of grains relative to the mixed zones of fine-grained plagioclase and micas that experience phase pinning. The competency contrast indicated by the different DRX mechanisms in quartz (GBM) and in plagioclase (BLG) suggests that quartz is the weaker phase and can accommodate strain through ease of recrystallization. The GBM recrystallization mechanism also helps explain the coarser grain size of quartz relative to plagioclase because driving force for recrystallization during GBM is driven by both strain energy and surface energy rather than strain energy alone (e.g., Platt and Behr, 2011; Stipp et al., 2002).

5.1.2. Dauphiné-twinned quartz sample

Microstructural observations indicate crystal plastic deformation of both plagioclase and quartz, but with strain partitioning into quartz that is both dynamically recrystallized and extensively Dauphiné twinned. In this sample, plagioclase porphyroclasts are rare because they are almost completely recrystallized, yet they are not disaggregated, and they retain their lens-like shapes (Fig. 5a and b). The presence of non-disaggregated, recrystallized porphyroclasts and some rare relict porphyroclast cores indicates rheologic competence of plagioclase relative to the recrystallized quartz that makes up the monomineralic S-fabric domains. In the S-fabric domains, quartz displays similar GBM microstructures to the untwinned quartz sample (Fig. 4e, f, 5a), and similarly,

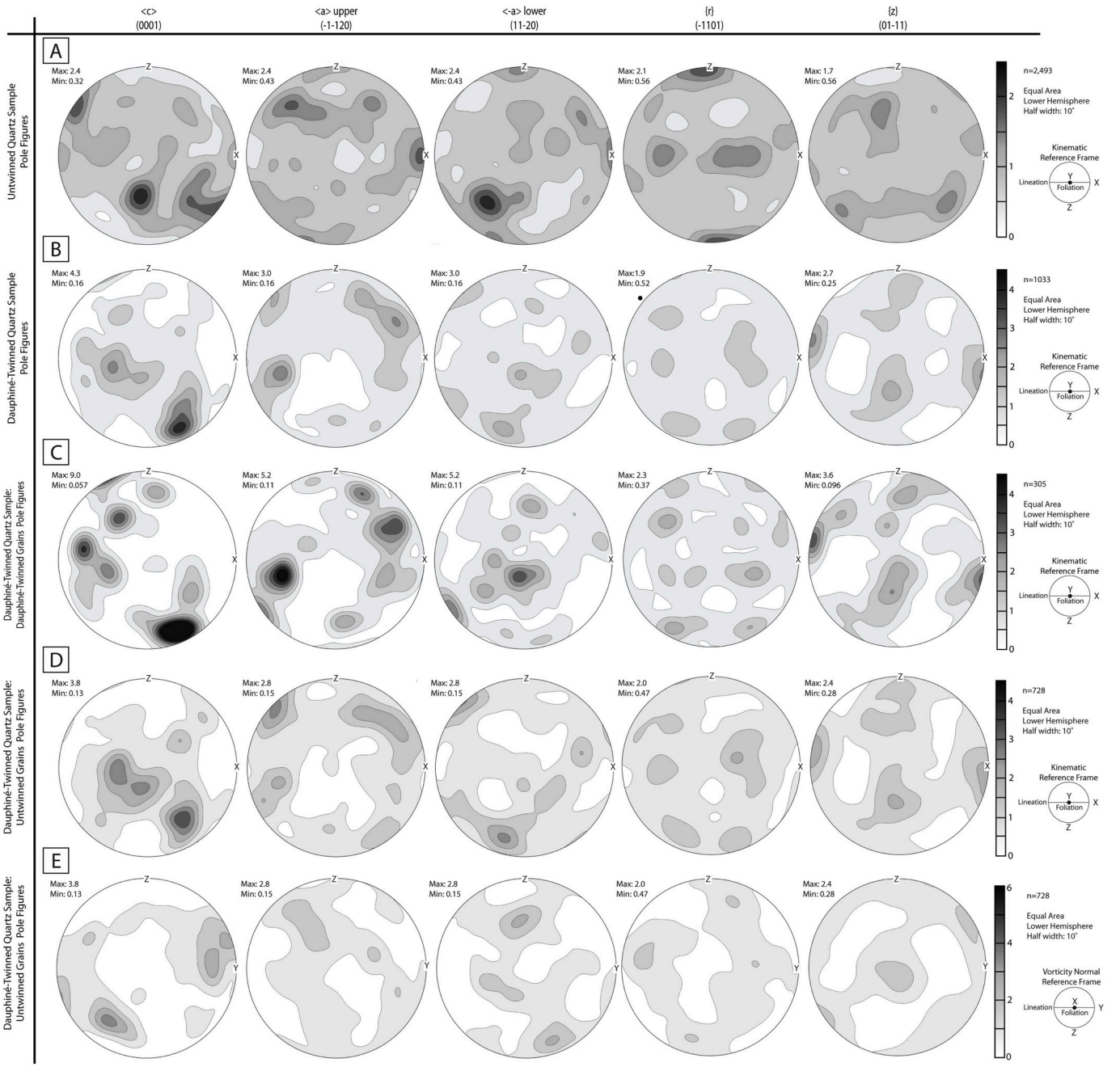

Fig. 7. Contoured pole figures of quartz crystallographic preferred orientations in the untwinned quartz sample and the Dauphiné-twinned quartz sample. Data are shown in the kinematic reference frame (a, b, c, d) and in the vorticity normal reference frame (e). a) Pole figure of quartz grain orientations from the EBSD map shown in Fig. 3 b) Pole figure of quartz grain orientations from the EBSD map shown in Fig. 5. The two subsets of (c) Dauphiné-twinned grain orientations and (d) untwinned grain orientations have different CPOs. See Supplemental Figure SP4 for the location of grains used in the quartz subsets of the Dauphiné-twinned quartz sample.

we interpret quartz as being the rheology-controlling mineral relative to plagioclase porphyroclasts and mixed plagioclase-mica zones. However, the prevalent Dauphiné twinning (Fig. 5a) indicates that deformation is accommodated in quartz in a way that is distinct from the untwinned quartz sample.

5.2. Interpretation of kinematic deformation geometry

The CVA plots show a distinct difference in the kinematic deformation geometry for 1) the untwinned and Dauphiné-twinned quartz samples, and 2) the constituent minerals within a given sample. The bulk CVA plot for the untwinned quartz sample (Fig. 6a) has a maximum that is consistent with simple shear-dominated transpression because the maximum clusters about the Y-axis, though it is strongly influenced by the strong plagioclase CVA pattern. Though the muscovite, quartz, and plagioclase CVA patterns all have maxima centered about the Y-axis also indicating simple shear-dominated transpression, the muscovite has an additional maximum that is centered on the X-axis, consistent with pure shear-dominated transpression. Similarly, the quartz CVA pattern forms a partial girdle along the X–Y axis that is also consistent with a transition towards pure shear-dominated transpression. In contrast, the bulk CVA pattern for the Dauphiné-twinned sample is consistent with triclinic transpression because the vorticity axis maximum is oblique to the lineation. The bulk CVA pattern also appears to be transitional between

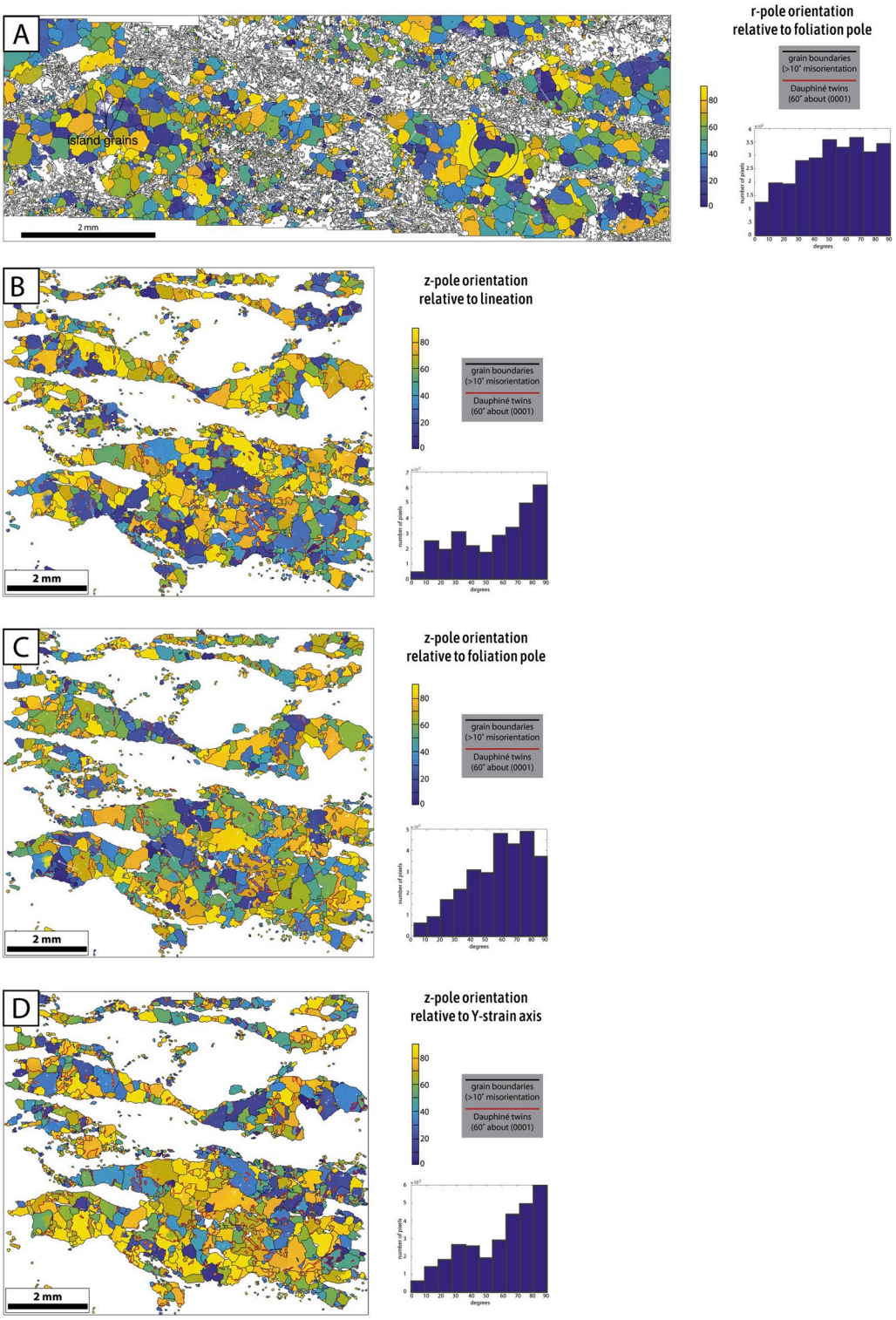

Fig. 8. EBSD maps of quartz bands in both samples showing the orientation of *r*- and *z*-poles relative to foliation and lineation. a) Map of the untwinned sample showing *r*-pole orientation relative to the foliation pole. Encircled region shows a grain with an *r*-pole sub-parallel to foliation pole being cut by a grain with an *r*-plane highly oblique to foliation pole. Island grains (black arrows) having *r*-poles at high angle to foliation pole are cut by and impinged upon by navy blue grains that have *r*-poles sub-parallel to foliation pole. White arrows show rare twin boundaries that separate navy blue parts of grains having *r*-poles sub-parallel to the foliation pole from the adjacent parts of the grains that have an *r*-pole oblique to foliation pole. b) Map of the Dauphiné-twinned sample showing *z*-pole relative to the lineation. c) Map of the Dauphiné-twinned sample showing *z*-pole orientation relative to the foliation pole. White arrows show where untwinned, navy blue grains cut or impinge upon Dauphiné-twinned grains. d) Map of the Dauphiné-twinned sample showing *z*-pole orientation relative to the Y strain axis. Each map includes a histogram showing the angular distribution of the orientations measured in degrees and the frequency with which it occurs as measured by number of pixels. (For interpretation of the references to color in this figure legend, the reader is referred to the Web version of this article.)

simple shear-dominated and pure shear-dominated transpression (Fig. 6e), where the bulk pattern is strongly influenced by the strong biotite CVA plot (Fig. 6f) and the quartz CVA plot (Fig. 6g). In this sample, the biotite CVA pattern is consistent with pure shear-dominated transpression, the plagioclase CVA pattern is consistent with simple shear-dominated transpression, and the quartz CVA pattern is intermediate between these two end members. A key point here is that the interpretation of 3D kinematic geometry from bulk CVA is more instructive when also viewed with constituent mineral CVA patterns because it yields insight into how simple and pure shear strain are partitioned between minerals.

In both samples, the muscovite and quartz CVA patterns are key in understanding the difference in 3D kinematic geometry between the samples. In both samples, the micas record more pure shear-dominated transpression relative to quartz, indicating strong kinematic partitioning by phase. However, the untwinned sample's muscovite and quartz CVA plots indicate that a greater degree of simple shear-dominated deformation was retained by this sample relative to the Dauphiné-twinned sample where the biotite CVA pattern shows dominantly pure shear-dominated transpression and the quartz CVA pattern is transitional between simple and pure shear-dominated transpression. We interpret the Dauphiné-twinned sample as having accommodated more pure shear-dominated transpression relative to the untwinned sample. Given the abundance of Dauphiné twins in the sample and the transitional nature of the quartz CVA fabric, we use the CVA patterns of the twinned and the untwinned grains within the sample (Fig. 6h and i) to explore the link between Dauphiné twin development and kinematic strain partitioning.

In the Dauphiné-twinned sample, the subset of twinned grains shows a CVA pattern consistent with the dominance of simple shear-dominated transpression, whereas the subset of untwinned grains has a transitional CVA pattern between simple and pure shear-dominated transpressional end members. Combined with the microstructures in the EBSD maps that show twinned grains being cut by and impinged upon by untwinned grains, this implies that the simple shear-dominated CVA fabrics develop prior to the pure shear-dominated fabrics. This sequence of fabric development is consistent with how strain accumulates in transpressional shear zones due to late stage pure shear accumulating strain more efficiently than early stage simple shear (e.g., Czeck and Hudleston, 2003; Fossen and Tikoff, 1993).

We interpret the strain partitioning between quartz and mica as a function of progressive transpressional deformation, where the micas record later stage pure shear-dominated deformation relative to quartz that captures more of the transition from simple to pure shear-dominated transpression. We interpret the micas as a weaker phase relative to quartz and plagioclase, consistent with an experimental study from Holyoke and Tullis (2006) where muscovite was the weakest phase compared to a deforming plagioclase and quartz framework. As the weakest phase, the micas are most likely to record the most recent kinematic geometry of the shear zone, which helps explain why the mica CVA patterns differ from those of quartz. Given the evidence from the micas that pure shear-dominated transpression was likely the most recent kinematic geometry, we interpret the Dauphiné-twinned grains as older microstructures associated with simple shear-dominated transpression, and we infer that they were less deformable relative to the untwinned grains that record pure shear-dominated transpression. We evaluate this interpretation further by close inspection of the pole figures for the Dauphiné-twinned and untwinned samples to compare the orientations of the twinned and untwinned grains.

5.3. CPO patterns and slip systems

The CPO patterns of the untwinned sample are consistent with high-temperature slip systems and with the completion of Dauphiné twinning. In the *c*-axis pole figure for all of the quartz grains (Fig. 7a), the locations of the maxima indicate that prism [*c*] slip is predominantly active, with weaker activation of prism <*a*>. The asymmetry of the prism [*c*] pattern is consistent with dextral sense of shear. In the positive rhomb *r* plane {-1101} pole figure, the orientation of the strongest maximum is parallel to the foliation pole, indicating that a set of positive rhomb planes are parallel to foliation. This orientation is consistent with studies of Dauphiné twinning that demonstrate that a set of *r*-poles become aligned normal to the foliation in response to compression (Menegon et al., 2011; Minor et al., 2018; Rahl et al., 2018). Though we observe this positive rhomb plane CPO pattern typically attributed to Dauphiné twinning in our untwinned sample, we interpret its presence as an indication that Dauphiné twinning has gone to completion in the sample such that the grains have been swept of nearly all twin boundaries.

The CPO patterns of the Dauphiné-twinned sample are more complicated to interpret. The pole figures derived from all quartz grains (Fig. 7b) are strongly influenced by the subset of twinned grains, so we consider the subsets of twinned and untwinned grains separately for our interpretations. In the subset of twinned grains (Fig. 7c), the *c*-axis pattern shows a maximum on the primitive that is oriented closer to the Z-axis relative to the positions of the maxima in the untwinned sample. This distinct difference in orientation implies the operation of basal <*a*> slip instead of the higher-temperature prism <*a*> and [*c*] slip systems. In the positive rhomb *r* plane {-1101} pole figure, there is a fabric minimum at the Z-axis, which is markedly different than the untwinned sample. Another primary difference is observed in the negative rhomb *z* {01–11} pole figure, where the strongest maximum shows the alignment of a set of *z*-poles nearly normal to the foliation pole. The negative rhomb *z* planes are regarded as elastically stiffer (Minor et al., 2018; Ohno et al., 2006; Rahl et al., 2018), and grains oriented with the stiffer *z* rhomb planes orthogonal to the greatest principal stress direction would be well-oriented for twinning (Rahl et al., 2018). The subordinate maximum near the Z-axis is consistent with this orientation, but not the strongest maximum in the pole figure. However in transpressional deformation, the greatest principal stress direction is not necessarily normal to the foliation because of the combined simple and pure shear components of deformation. Instead, the negative rhomb *z* plane orientations in the twinned grains corresponding to the strongest maximum in the pole figure imply that there was a component of shortening parallel to what is now the lineation direction. A component of shortening normal to the current Y-Z reference plane might also help explain the somewhat anomalous *c*-axis and negative rhomb *z* pole figure patterns in the twinned grain subset; if these CPO patterns were interpreted relative to an older foliation parallel to the Y-Z plane, the *c*-axis pole figure would be consistent with prism [*c*] slip with a sinistral sense of shear instead of the lower-temperature basal<*a*> slip system, and the twinned grains would have a *z*-plane optimally oriented for twinning. The higher temperature prism [*c*] slip system is consistent with the prism slip systems we interpret in the untwinned sample, and it is also more consistent with the high-temperature GBM microstructures we observe in the sample that typically result from prism <*a*> or prism [*c*] slip (e.g., Langille et al., 2010).

The untwinned grains subset in the Dauphiné-twinned sample has a CPO pattern that strongly resembles that of the twinned grains subset (compare Fig. 7d and c, respectively). In particular, the positive rhomb *r* and negative rhomb *z* pole figures are remarkably similar in geometry to those of the twinned grain subset, though the strength of the strongest maximum in the negative rhomb *z* pole figure is subdued in the untwinned subset. However, the quartz CVA pattern of the untwinned grains shows a greater component of pure shear-dominated deformation relative to the twinned grains subset, which requires that the CPO data should be interpreted with respect to slip systems in the vorticity normal reference frame (see bottom of Fig. 6). This is distinct from the conventional kinematic reference frame only in the case of pure shear-dominated transpression [e.g., Michels et al., 2015; Giorgis et al., 2016]. When viewed in the vorticity normal reference frame, the quartz *c*-axis pattern of the untwinned grains has a maximum on the primitive near the Y-axis that indicates prism [*c*] slip, (Fig. 7e), the highest

temperature slip system in quartz [e.g., Mainprice et al., 1986; Law, 2014]. The asymmetry in the prism [*c*] pattern is consistent with sinistral sense of shear.

5.4. Interpretation of quartz r-pole and z-pole orientation maps

The map of *r*-pole orientation relative to foliation pole for the untwinned sample (Fig. 8a) shows that navy blue grains having an *r*-plane sub-parallel to foliation both cut and are cut by grains that are differently oriented, suggesting that there is temporal variability in the grains' acquisition of this ideal orientation. These mutually cross-cutting relations also suggest that development of the positive rhomb *r* {-1101} CPO cannot be explained solely by the growth of navy blue grains at the expense of other, less ideally oriented grains. Additional insight is afforded by comparing the *r*-pole orientation map to the mis2mean EBSD map shown in Fig. 3d; ideally oriented navy blue grains are cut by less ideally oriented grains having lower intragrain misorientation, indicating that grain boundary mobility is a function of both strain energy and crystallographic orientation. In addition, the rare Dauphiné twin boundaries commonly separate parts of grains with contrasting intragrain misorientation, with a convex shape into the more misoriented part of the grain. Yet, the side of the twin boundary that is less misoriented does not always correspond to an ideally oriented navy blue grain in Fig. 8b. Here, too, Dauphiné twin mobility may be influenced by strain energy. We therefore attribute the positive rhomb *r* CPO in this sample to the nucleation of Dauphiné twins in response to a component of shortening normal to the foliation. The twin boundaries then sweep through grains and go to completion to minimize strain energy, with the end result being that the grains retain the CPO but not many twin boundaries.

The maps of *z*-pole orientation relative to the lineation and to the foliation pole for the twinned sample (Fig. 8b and c) highlight important differences in the deformability of the Dauphiné-twinned and untwinned grains. In the *z*-pole orientation relative to lineation map (Fig. 8b), twinned grains feature prominently in the navy blue grain population, and as with the twinned grains in the *r*-pole map, the twin boundaries commonly juxtapose parts of grains that have different amounts of intragrain misorientation (compare Fig. 5d with Fig. 8b). Here, too, twin development also seems to be influenced by strain energy. Curiously, these twinned navy blue grains have their strongest negative rhomb *z*-pole maximum oriented parallel to lineation, indicating that this stiffer, less compliant direction is parallel to lineation. This *z*-pole orientation is inconsistent with the Dauphiné twins forming from shortening normal to the foliation, as grains with their *z*-pole oriented normal to foliation would be more prone to twinning (Rahl et al., 2018). This suggests the shortening direction may have evolved since the time that the Dauphiné twins formed in the grains with a *z*-pole parallel to lineation. Additional insight is gained from the *z*-pole orientation relative to the foliation pole map (Fig. 8c), where most of the navy blue grains are untwinned and are ideally oriented for nucleating Dauphiné twins from shortening normal to the foliation. The paucity of Dauphiné twins in the grains that are well-oriented for twinning suggests that twinning may have gone to completion in these untwinned grains. This interpretation is supported by an *r*-pole maximum near the Z-strain axis in the untwinned grains pole figure (Fig. 7d). Further, these untwinned grains that have a *z*-pole normal to the foliation cut and/or impinge upon the Dauphiné twinned grains, demonstrating that the Dauphiné twinning is an older microstructure relative to the untwinned grains that impinge upon them. We interpret that the untwinned quartz could more easily accommodate deformation compared to the less deformable, Dauphiné-twinned quartz grains.

5.5. Conditions of GSZ deformation

The dynamic recrystallization microstructures, inferred slip systems, and independent measures of temperature together are consistent with amphibolite facies GSZ shear zone deformation temperatures. GBM microstructures similar to the ones we observe in our samples are typically developed at temperatures ranging from 550°-650 °C in naturally deformed quartz [e.g., Stipp et al., 2002], and the *c*-axis patterns we observe in the pole figures are also correlative with GBM at high temperatures [e.g., Stipp et al., 2002; Law, 2014]. In particular, the transition from prism <*a*> to prism [*c*] slip is associated with temperatures of ~630 ± 30 °C (Fig. 8a) (Law, 2014; Stipp et al., 2002), and the appearance of the prism [*c*] maxima is attributed to very high temperatures of deformation, typically in excess of 630–650 °C (Mainprice et al., 1986; Stipp et al., 2002). Though it has been shown that quartz CPO development is not solely a function of temperature and can vary with strain rate and water weakening (Heilbronner and Tullis, 2006; Law, 2014; Muto et al., 2011; Toy et al., 2008; Tullis et al., 1973), we note that there is overlap in the temperature estimates based on our samples' microstructures and CPO patterns. In addition, the independent measures of deformation temperature from Zr-in-titanite thermometry of the Lake Te Anau mylonites yield temperatures of 610–660 °C (Buriticá et al., 2019). We therefore estimate that quartz fabric development in the Dauphiné-twinned sample developed at ~610-660 °C in the GSZ, consistent with the amphibolite facies temperatures interpreted by other independent thermometers (Scott et al., 2011).

5.6. Dauphiné twinning records progressive inclined transpression in the GSZ

The Grebe Shear Zone is a transpressional shear zone, and our foliation and lineation measurements from the Lake Te Anau mylonites allow the further classification of the GSZ as a zone of inclined transpression. In inclined transpression, the foliation deviates from vertical and the lineations can range from horizontal to vertical in plunge (Czeck and Hudleston, 2003; Jones et al., 2004), all within a shear zone that has boundaries oblique to the shear zone foliation. Our untwinned sample has a more southern strike (185°), a shallower dip (70°), and a shallower plunge of lineation (19°) relative to the Dauphiné-twinned sample. We reconcile the differences in these foliation and lineation geometries by interpreting the locations of the samples within the GSZ relative to the shear zone boundaries and the deflected shear zone foliation resulting from sinistral shear sense (Fig. 9). A key element of this model is that the untwinned sample lies close to the shear zone boundary, where the foliation makes a small angle with the shear zone boundary and the lineation approaches parallelism with the horizontal strike-slip simple shear component of motion. In contrast, the Dauphiné-twinned sample lies closer to the middle of the shear zone strand where the trace of foliation is more oblique to the shear zone boundary and the lineation plunges more moderately. 'insert Fig. 9'.

The locations of the samples within the GSZ provides an explanation for the relative amounts of simple shear and pure shear deformation accommodated by the samples. In the untwinned sample, the lineation is almost strike-parallel, which makes the deformation tend towards end-member strike-slip strain, which would result in a nearly monoclinic strain symmetry (Jiang et al., 2001; Jones et al., 2004; Lin et al., 1998). The monoclinic strain symmetry is reflected in the bulk CVA pattern that shows simple-shear dominated transpression where the vorticity axis is perpendicular to lineation (Fig. 6a). In contrast, the Dauphiné-twinned sample has a steeper and moderate plunge of the lineation, and in inclined transpression, intermediate values of pitch are associated with more recognizably triclinic strain symmetry. This is reflected in the bulk CVA pattern that shows the vorticity axis oriented obliquely to lineation, and shows kinematic deformation geometry transitional between simple and pure shear-dominated transpression (Fig. 6e). The triclinic strain symmetry requires that all three axes of the finite strain ellipsoid have a component of vorticity and continuously change orientation during progressive inclined transpression.

Progressive inclined transpression requires re-orientation of foliation and lineation in response to the progressive rotation of the finite strain

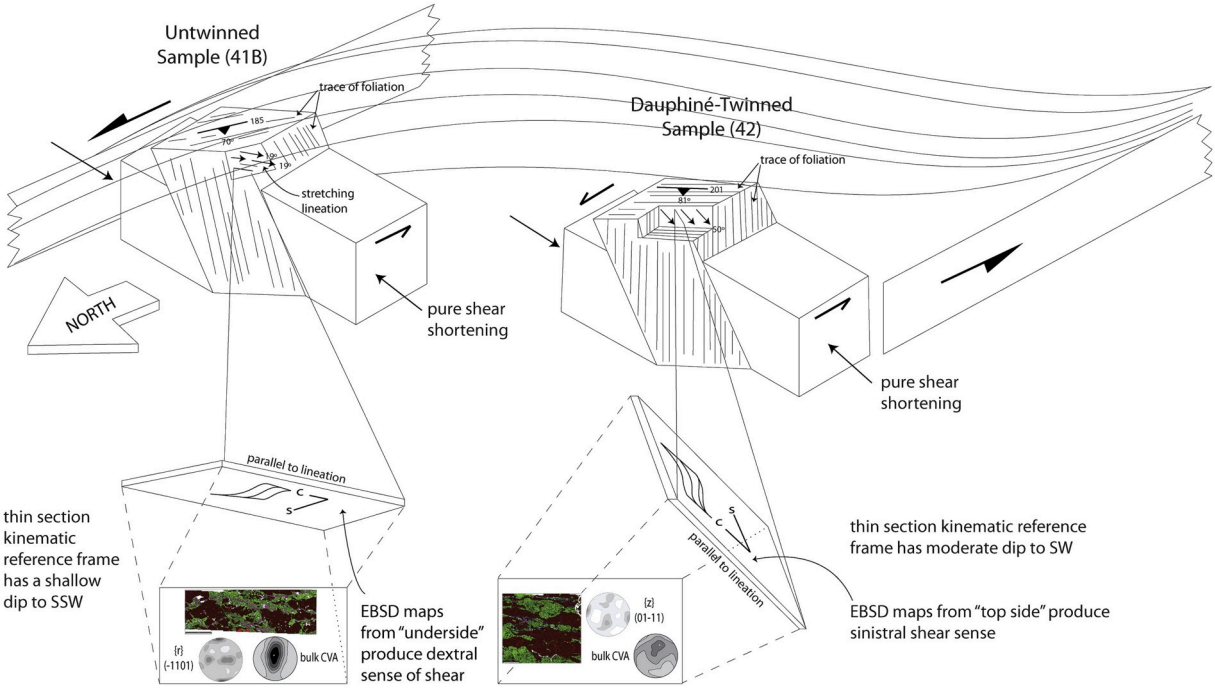

Fig. 9. Schematic block diagram showing location of samples within the Grebe Shear Zone relative to the shear zone boundaries and relative to the form lines for the traces of shear zone foliation. The GSZ is a zone of inclined transpression that accommodates sinistral strike-slip motion and E-W shortening. The locations of both thin section billets relative to the local kinematic reference frame is indicated by the profiles parallel to lineation for each sample. The thin section billet cut parallel to lineation and perpendicular to foliation in the untwinned sample has a shallow dip to the SSW, whereas the thin section billet cut from the Dauphiné-twinned sample has a more moderate dip to the SW. The untwinned sample thin section was cut from the downward-facing "underside" of the billet, explaining the apparent dextral shear sense in this sample; if the thin section was cut from the upward-facing side of the billet, the maps and microstructures would show sinistral sense motion. For the Dauphiné-twinned sample, the thin section was cut from the up-facing "top side" of the billet, showing the sinistral sense of shear that is consistent with the shear sense in the GSZ. For each sample, a representative EBSD phase map, pole figure, and bulk CVA pattern to view these data with respect to the broader geographic and structural reference frame. Block diagrams modified after Jones et al. (2004).

ellipsoid. The nature of the re-orientation is strongly dependent on strain path and can be highly variable, but for most strain paths the lineation pitch will change significantly, even with small amounts of shortening (Jones et al., 2004). The re-orientation of lineation is accompanied by re-orientation of foliation, resulting in partial to full overprinting of earlier fabric orientations. We see evidence for this in the twinned grains of the Dauphiné-twinned sample in the form of *z*-pole orientations parallel to lineation and a low-temperature quartz slip system when viewed with respect to the current foliation and lineation orientations (Fig. 7c). The *z*-pole and *c*-axis fabrics in this subset of grains suggest that an earlier foliation oriented nearly orthogonal to the current foliation was overprinted with the aid of GBM recrystallization, leaving the anomalous CPO patterns in the twinned grains as the relict structural evidence.

Our model invokes strain heterogeneity as a consequence of triclinic progressive inclined transpression to explain the differences in how the untwinned and Dauphiné-twinned sample accommodate deformation. There is an element of similarity between our model and that of Goodwin and Tikoff (2002) in that we recognize shear zone domains in which lineation orientation is different as a consequence of strain partitioning, but our models differ in three main ways. First, Goodwin and Tikoff (2002) assume monoclinic transpression where strain is partitioned into *C*-domains that have horizontal lineations and *S*-domains that have vertical lineations. In our model, our samples deform in triclinic inclined transpression, which tends to produce obliquely plunging lineations, though vertical and horizontal lineations are possible. A second difference is that in the Goodwin and Tikoff (2002) model, strain partitioning into *S*- and *C*-domains requires that vertical and horizontal lineations develop coevally and maintain their orientation in the shear zone, but in progressive inclined transpression, there is a temporal evolution of lineation orientation. The last difference that we emphasize is that the Goodwin and Tikoff (2002) model proposes kinematic partitioning between domains such that *S*- and *C*-fabrics and their respective vertical and horizontal lineations accommodate end-member pure and simple shear strains, respectively, whereas in our inclined transpression model the kinematic partitioning of strain does not manifest in spatial separation of end-member pure and simple shear deformation. Rather, a sample's position within the inclined transpressional shear zone influences the relative proportions of pure and simple shear deformation accommodated by the sample. In our model, the untwinned sample on the margins of the GSZ is dominated by more simple-shear deformation, whereas the Dauphiné-twinned sample located within the middle of GSZ accommodates a greater component of pure shear shortening relative to the untwinned sample.

We conclude that Dauphiné twinning formed as a mechanical response to a component of pure shear shortening during the early stages of inclined transpression. In the untwinned sample, we interpret the current foliation as similar in orientation to the foliation in which Dauphiné twins were formed and have since gone to completion. The nearly orthogonal angle between the sample's foliation and the shortening direction across the GSZ results in compression nearly orthogonal to the foliation, consistent with the CPO pattern showing *r*-pole maxima normal to the foliation (Fig. 9). This is similar to other studies of Dauphiné twinning where a set of *r*-poles become aligned normal to the foliation in response to the compression (Menegon et al., 2011; Minor et al., 2018; Rahl et al., 2018). The foliation in the untwinned sample is also nearly parallel to the shear zone boundary and the lineation is gently plunging, indicating that a large amount of simple shear strain is resolved along the foliation, which is also reflected in the bulk CVA pattern that is consistent with simple shear-dominated transpression (Fig. 9). The Dauphiné-twinned sample's position within the GSZ and the obliquity of its foliation relative to the pure shear shortening

direction (Fig. 9) suggests the likelihood of progressive fabric re-orientation during progressive inclined transpression, which is reflected in the bulk CVA pattern indicating triclinic transpression. Evidence for an older foliation oriented at high angle to the present-day foliation includes anomalous *z*-pole and *c*-axis CPO patterns of Dauphiné-twinned grains that would be more likely to form in response to shortening and sinistral shear across a foliation oriented nearly parallel to the current Y-Z plane rather than the current foliation in the X-Z plane. These twinned grains are commonly cut or impinged upon by untwinned grains indicating the Dauphiné twins are an older microstructure developed during an earlier stage of inclined transpression. This older foliation was largely overprinted by the most recent foliation that defines the present-day X-Z plane in the sample.

The partial overprinting of the Dauphiné-twinned sample is particularly useful for interpreting how progressive fabric reorientation is achieved. After the Dauphiné twins formed, GBM DRX promoted foliation re-orientation, producing a population of untwinned grains that became well-oriented for deformation during the later stages of transpression. We interpret the untwinned grains in the Dauphiné-twinned sample as evidence that some mechanical twins produced during early transpression became mobile and went to completion with the aid of GBM [e.g., Piazolo et al., 2005], and these grains are well-aligned for high-temperature prism [*c*] slip systems with respect to the current orientation of foliation when viewed in the vorticity normal reference frame. The changing orientation of the foliation made it possible for these grains to grow at the expense of extensively twinned grains with less compliant orientations of *z*-planes. The growth of well-oriented grains at the expense of those in unfavorable orientations has been shown to occur in other studies of GBM in quartz (Little et al., 2015) and in ice (Qi et al., 2017). We conclude that GBM helped strain become partitioned into the untwinned grains in the later stages of transpression.

The relative deformability of the untwinned and Dauphiné-twinned grains in the Dauphiné-twinned sample can be integrated with the CVA pattern interpretations to understand temporal variations in kinematic geometry due to competence contrasts. We attribute the differences in the CVA patterns of the untwinned grains relative to Dauphiné-twinned grains to be a result of the relative deformability of these grain populations. The Dauphiné-twinned grains have a *z*-plane normal to the lineation (Fig. 7c), which makes them behave more rigidly compared to the untwinned grains (Fig. 7d and e). The untwinned grains that have an *r*-plane parallel to foliation have lower mis2mean values than many twinned grains (Fig. 5d) and are more deformable. When twinning goes to completion in the untwinned grains, they can easily accommodate the shift to pure shear-dominated transpression as recorded by the CVA pattern. We conclude that Dauphiné twinning formed at the transition from simple shear to pure shear-dominated transpression; the twinned grains became less deformable with continued pure shear-dominated transpression, and as a result, the pure shear component of transpression was partitioned into untwinned grains.

Strain localization was maintained along this part of the GSZ in large part through GBM DRX such that the untwinned grains accommodated the changing sense of kinematic deformation geometry. The vorticity axes of Dauphiné twinned grains show that they preserve early simple shear-dominated transpression, but the Dauphiné twinning developed in response to compression parallel to the current lineation, marking the onset of pure shear-dominated transpression. Continued accumulation of the pure shear component of transpression coincided with foliation re-orientation and continued GBM, producing the population of untwinned quartz grains in which twinning went to completion. Strain became largely partitioned into these untwinned quartz grains as they grew at the expense of Dauphiné-twinned grains and continued to sustain deformation by GBM DRX, forming CVA patterns associated with late-stage, pure shear-dominated transpression. We conclude that the ease of recrystallization in these more deformable grains acted to maintain localization of the shear zone.

There are three major implications of our work: 1) the effectiveness of Dauphiné twinning in promoting strain localization is strongly influenced by the timing of twin formation relative to an evolving kinematic deformation geometry during inclined transpression, 2) the dynamic recrystallization mechanism occurring in tandem with Dauphiné twinning exerts a primary control on the effectiveness of strain localization, and 3) CVA analysis is a useful tool for understanding how strain is partitioned during progressive inclined transpression. Regarding implication #1, Dauphiné twinning developed early in the development of the transpressional shear zone, and only those grains that had achieved twin completion, and were well-oriented with respect to the re-orienting foliation were able to accommodate further strain. These outcomes suggest that caution should be used when considering Dauphiné twinning as a potential piezometer because the timing of twinning development is critical in relating stress estimates to shear zone evolution. Regarding implication #2, our work shows that GBM promotes strain localization in untwinned grains where twinning has gone to completion, rather than in grains where Dauphiné twin microstructures are well preserved. This is in striking contrast to the interplay of SGR and Dauphiné twinning, where dynamic recrystallization preferentially occurs within narrow bands of preserved *r*-twins (Menegon et al., 2011). Thus the mobility of Dauphiné twin boundaries during GBM is key in controlling strain localization, particularly in transpressional shear zones. Regarding implication #3, our work demonstrates the utility of CVA analysis in investigating how transpressional deformation is partitioned between different grain populations of an individual mineral phase, and between different minerals. Together, microstructural and CVA analysis reveal temporal variations in kinematic deformation geometry that yield valuable insight into the evolution of regional-scale shear zones.

6. Conclusions

Our microstructural, EBSD, CVA, and misorientation analyses of the untwinned quartz sample and Dauphiné-twinned quartz sample reveal an evolution in the kinematic deformation geometry of the GSZ during inclined transpression, where the geometry evolved from simple shear- to pure shear-dominated transpression. In both samples, quartz underwent high-temperature deformation via GBM DRX. The similar CVA patterns of micas in both samples suggests similar behavior of these minerals within the shear zone, whereas the different quartz CVA patterns indicate that quartz accommodated the evolving 3D deformation geometry differently depending on the presence and mobility of Dauphiné twins. The Dauphiné-twinned grains record early simple shear-dominated transpression, and the untwinned grains in the Dauphiné-twinned sample record late-stage pure shear-dominated deformation. CPO patterns indicate activation of prism <*a*> and prism [*c*] slip in the untwinned sample, and prism [c] slip in the Dauphiné-twinned sample. The microstructures and quartz CPO patterns in both samples are consistent with the deformation temperatures determined by Zr-in-titanite thermometry (610°-660 °C) for other Lake Te Anau mylonites from the GSZ. Our work also demonstrates the utility of CVA analysis in interpreting how strain partitioning and microstructural development relates to temporal variations in kinematic deformation geometry of inclined transpressional shear zones.

Data availability

Datasets related to this article can be found at: https://doi.org/10.17632/dg7kv5mcv3.1, an open-source online data repository hosted at Mendeley Data.

Declaration of competing interest

The authors declare that they have no known competing financial interests or personal relationships that could have appeared to influence the work reported in this paper.

CRediT authorship contribution statement

Courtney McGinn: Conceptualization, Software, Investigation, Data curation, Writing - original draft, Visualization, Funding acquisition. **Elena A. Miranda:** Conceptualization, Methodology, Software, Validation, Formal analysis, Investigation, Resources, Data curation, Writing - original draft, Writing - review & editing, Visualization, Supervision, Project administration, Funding acquisition. **Lonnie J. Hufford:** Validation, Investigation.

Acknowledgements

This work was supported by the National Science Foundation award #EAR 1650219 to E.A. Miranda, and by three student awards to C.A. McGinn from the CSUN Dept. of Geological Sciences: the Hanna Summer Student Research Award, the Hanna Graduate Fellowship, and the Larry Collins Scholarship. We thank Andrew Cross and Zachary Michels for assistance with the MTEX scripts. We thank the New Zealand Department of Land Conservation for permission to sample in Fiordland, GNS Science in Dunedin for access to facilities to process our samples, and Joshua Schwartz for assistance and support with sampling in the field. We gratefully acknowledge Sabine Faulhaber and Emily Chin for assistance with EBSD analyses at UCSD. We are also appreciative of the thorough and constructive reviews by L.F.G. Morales and J. Rahl that helped improve this manuscript.

Appendix A. Supplementary data

Supplementary data to this article can be found online at https://doi.org/10.1016/j.jsg.2020.103980.

References

Allibone, A.H., Jongens, R., Scott, J.M., Tulloch, A.J., Turnbull, I.M., Cooper, A.F., Powell, N.G., Ladley, E.B., King, R.P., Rattenbury, M.S., 2009a. Plutonic rocks of the Median Batholith in eastern and central Fiordland , New Zealand : field relations , geochemistry , correlation , and nomenclature. N. Z. J. Geol. Geophys. 52, 101–148. https://doi.org/10.1080/00288300909509882.

Allibone, A.H., Jongens, R., Turnbull, I.M., Milan, L.A., Daczko, N.R., DePaoli, M.C., Tulloch, A.J., 2009b. Plutonic rocks of Western Fiordland, New Zealand: field relations, geochemistry, correlation, and nomenclature. N. Z. J. Geol. Geophys. 52, 379–415. https://doi.org/10.1080/00288306.2009.9518465.

Allibone, A.H., Tulloch, A.J., 2008. Early cretaceous dextral transpressional deformation within the median batholith, Stewart Island, New Zealand. N. Z. J. Geol. Geophys. 51, 115–134. https://doi.org/10.1080/00288300809509854.

Bachmann, F., Hielscher, R., Schaeben, H., 2010. Texture analysis with MTEX - free and open source software toolbox. Solid State Phenom. 160, 63–68. https://doi.org/10.4028/www.scientific.net/SSP.160.63.

Buritica, L., 2018. Temporal and Spatial Variations in Magmatism and Transpressional Deformation in the Middle to Lower-Crust of a Cretaceous Arc, Median Batholith, Fiordland, New Zealand. MSc Thesis. CSU-Northridge.

Buriticá, L.F., Schwartz, J.J., Klepeis, K.A., Miranda, E.A., Tulloch, A.J., Coble, M.A., Kylander-Clark, A.R.C., 2019. Temporal and spatial variations in magmatism and transpression in a Cretaceous arc, Median Batholith, Fiordland, New Zealand. Lithosphere 11, 652–682. https://doi.org/10.1130/L1073.1.

Cross, A.J., Prior, D.J., Stipp, M., Kidder, S., 2017. The recrystallized grain size piezometer for quartz: an EBSD-based calibration. Geophys. Res. Lett. https://doi.org/10.1002/2017GL073836.

Czeck, D.M., Hudleston, P.J., 2003. Testing models for obliquely plunging lineations in transpression: a natural example and theoretical discussion. J. Struct. Geol. 25, 959–982. https://doi.org/10.1016/S0191-8141(02)00079-2.

Fossen, H., Tikoff, B., 1993. The deformation matrix for simultaneous simple shearing, pure shearing and volume change, and its application to transpression-transtension tectonics. J. Struct. Geol. 15, 413–422. https://doi.org/10.1016/0191-8141(93)90137-Y.

Giorgis, S., Michels, Z., Dair, L., Braudy, N., Tikoff, B., 2016. Kinematic and vorticity analyses of the western Idaho shear zone , USA. Lithosphere 9, 223–234. https://doi.org/10.1130/L518.1.

Goodwin, L.B., Tikoff, B., 2002. Competency contrast, kinematics, and the development of foliations and lineations in the crust. J. Struct. Geol. 24, 1065–1085. https://doi.org/10.1016/S0191-8141(01)00092-X.

Heilbronner, R., Tullis, J., 2006. Evolution of c axis pole figures and grain size during dynamic recrystallization : results from experimentally sheared quartzite. J. Geophys. Res. 111, 1–19. https://doi.org/10.1029/2005JB004194.

Hielscher, R., Schaeben, H., 2008. A novel pole figure inversion method: specification of the MTEX algorithm. J. Appl. Crystallogr. 41, 1024–1037. https://doi.org/10.1107/S0021889808030112.

Hirth, G., Tullis, J., 1992. Dislocation creep regimes in quartz aggregates. J. Struct. Geol. 14, 145–159. https://doi.org/10.1016/0191-8141(92)90053-Y.

Holyoke, C.W., Tullis, J., 2006. The interaction between reaction and deformation : an experimental study using a biotite + plagioclase + quartz gneiss. J. Metamorph. Geol. 24, 743–762. https://doi.org/10.1111/j.1525-1314.2006.00666.x.

Jiang, D., Lin, S., Williams, P.F., 2001. Deformation path in high-strain zones, with reference to slip partitioning in transpressional plate-boundary regions. J. Struct. Geol. 23, 991–1005. https://doi.org/10.1016/S0191-8141(00)00170-X.

Jones, R.R., Holdsworth, R.E., Clegg, P., McCaffrey, K., Tavarnelli, E., 2004. Inclined transpression. J. Struct. Geol. 26, 1531–1548. https://doi.org/10.1016/j.jsg.2004.01.004.

Klepeis, K.A., Clarke, G.L., Gehrels, G., Vervoort, J., 2004. Processes controlling vertical coupling and decoupling between the upper and lower crust of orogens: results from Fiordland, New Zealand. J. Struct. Geol. 26, 765–791. https://doi.org/10.1016/j.jsg.2003.08.012.

Klepeis, K.A., Schwartz, J., Stowell, H., Tulloch, A., 2016. Gneiss domes, vertical and horizontal mass transfer, and the initiation of extension in the hot lower-crustal root of a continental arc, Fiordland, New Zealand. Lithosphere 8. https://doi.org/10.1130/L490.1.

Langille, J.M., Jessup, M.J., Cottle, J.M., Newell, D., Seward, G., 2010. Kinematic evolution of the ama drime detachment: insights into orogen-parallel extension and exhumation of the ama drime massif, TibeteNepal. J. Struct. Geol. 32, 900–919. https://doi.org/10.1016/j.jsg.2010.04.005.

Law, R.D., 2014. Deformation thermometry based on quartz c-axis fabrics and recrystallization microstructures: a review. J. Struct. Geol. 66, 129–161. https://doi.org/10.1016/j.jsg.2014.05.023.

Lin, S., Jiang, D., Williams, P.F., 1998. Transpression (or transtension) zones of triclinic symmetry: natural example and theoretical modelling. Geol. Soc. Spec. Publ. 135, 41–57. https://doi.org/10.1144/GSL.SP.1998.135.01.04.

Little, T.A., Prior, D.J., Toy, V.G., Lindroos, Z.R., 2015. The link between strength of lattice preferred orientation, second phase content and grain boundary migration: a case study from the Alpine Fault zone, New Zealand. J. Struct. Geol. 81, 59–77. https://doi.org/10.1016/J.JSG.2015.09.004.

Lloyd, G.E., 2004. Microstructural evolution in a mylonitic quartz simple shear zone: the significant roles of dauphine twinning and misorientation. Geol. Soc. London, Spec. Publ. 224, 39–61. https://doi.org/10.1144/GSL.SP.2004.224.01.04.

Mainprice, D., Bouchez, J.L., Blumenfeld, P., Tubià, J.M., 1986. Dominant c slip in naturally deformed quartz: implications for dramatic plastic softening at high temperature. Geology 14, 819–822. https://doi.org/10.1130/0091-7613(1986)14<819:DCSIND>2.0.CO;2.

Marcotte, S.B., Klepeis, K.A., Clarke, G.L., Gehrels, G., Hollis, J.A., 2005. Intra-arc transpression in the lower crust and its relationship to magmatism in a Mesozoic magmatic arc. Tectonophysics 407, 135–163. https://doi.org/10.1016/j.tecto.2005.07.007.

Menegon, L., Piazolo, S., Pennacchioni, G., 2011. The effect of Dauphiné twinning on plastic strain in quartz. Contrib. Mineral. Petrol. 161, 635–652. https://doi.org/10.1007/s00410-010-0554-7.

Michels, Z.D., Kruckenberg, S.C., Davis, J.R., Tikoff, B., 2015. Determining vorticity axes from grain-scale dispersion of crystallographic orientations. Geology 43, 803–806. https://doi.org/10.1130/G36868.1.

Minor, A., Rybacki, E., Sintubin, M., Vogel, S., Wenk, H.-R., 2018. Tracking mechanical Dauphiné twin evolution with applied stress in axial compression experiments on a low-grade metamorphic quartzite. J. Struct. Geol. 112, 81–94. https://doi.org/10.1016/j.jsg.2018.04.002.

Morales, L.F.G., Lloyd, G.E., Mainprice, D., 2014. Fabric transitions in quartz via viscoplastic self-consistent modeling part I: axial compression and simple shear under constant strain. Tectonophysics 636, 52–69. https://doi.org/10.1016/J.TECTO.2014.08.011.

Morales, L.F.G., Mainprice, D., Lloyd, G.E., Law, R.D., 2011. Crystal fabric development and slip systems in a quartz mylonite: an approach via transmission electron microscopy and viscoplastic self-consistent modelling. Geol. Soc. London, Spec. Publ. 360, 151–174. https://doi.org/10.1144/SP360.9.

Mortimer, N., Tulloch, A.J., Spark, R.N., Walker, N.W., Ladley, E., Allibone, A., Kimbrough, D.L., 1999. Overview of the median batholith, New Zealand : a new interpretation of the geology of the median tectonic zone and adjacent rocks. J. Afr. Earth Sci. 29, 257–268. https://doi.org/10.1016/S0899-5362(99)00095-0.

Muto, J., Hirth, G., Heilbronner, R., Tullis, J., 2011. Plastic anisotropy and fabric evolution in sheared and recrystallized quartz single crystals. J. Geophys. Res. 116, 1–18. https://doi.org/10.1029/2010JB007891.

Neumann, B., 2000. Texture development of recrystallised quartz polycrystals unravelled by orientation and misorientation characteristics. J. Struct. Geol. 22, 1695–1711. https://doi.org/10.1016/S0191-8141(00)00060-2.

Ohno, I., Harada, K., Yoshitomi, C., 2006. Temperature variation of elastic constants of quartz across the α - β transition. Phys. Chem. Miner. 33, 1–9. https://doi.org/10.1007/s00269-005-0008-3.

Pehl, J., Wenk, H.-R., 2005. Evidence for regional Dauphine twinning in quartz from the Santa Rosa mylonite zone in Southern California. A neutron diffraction study. J. Struct. Geol. 27, 1741–1749. https://doi.org/10.1016/j.jsg.2005.06.008.

Piazolo, S., Prior, D.J., Holness, M.D., 2005. The use of combined cathodoluminescence and EBSD analysis : a case study investigating grain boundary migration mechanisms in quartz. J. Microsc. 217, 152–161. https://doi.org/10.1111/j.1365-2818.2005.01423.x.

Platt, J.P., Behr, W.M., 2011. Grainsize evolution in ductile shear zones : implications for strain localization and the strength of the lithosphere. J. Struct. Geol. 33, 537–550. https://doi.org/10.1016/j.jsg.2011.01.018.

Qi, C., Goldsby, D.L., Prior, D.J., 2017. The down-stress transition from cluster to cone fabrics in experimentally deformed ice. Earth Planet Sci. Lett. https://doi.org/10.1016/j.epsl.2017.05.008.

Rahl, J.M., McGrew, A.J., Fox, J.A., Latham, J.R., Gabrielson, T., 2018. Rhomb-dominated crystallographic preferred orientations in incipiently deformed quartz sandstones : a potential paleostress indicator for quartz-rich rocks. Geology 46, 195–198. https://doi.org/10.1130/G39588.1.

Rattenbury, M., Isaac, M., 2012. The QMAP 1:250 000 geological map of New Zealand project. N. Z. J. Geol. Geophys. 55, 393–405. https://doi.org/10.1080/00288306.2012.725417.

Ringwood, M., 2018. Temporal and Spatial Patterns in a Mesozoic Magmatic Arc: Insights from Fiordland, New Zealand. CSU-Northridge.

Schwartz, J.J., Klepeis, K.A., Sadorski, J.F., Stowell, H.H., Tulloch, A.J., Coble, M.A., 2017. The tempo of continental arc construction in the Mesozoic Median Batholith, Fiordland, New Zealand. Lithosphere. https://doi.org/10.1130/L610.1. L610.1.

Scott, J.M., 2013. A review of the location and significance of the boundary between the Western Province and Eastern Province , New Zealand. N. Z. J. Geol. Geophys. 56, 276–293. https://doi.org/10.1080/00288306.2013.812971.

Scott, J.M., Cooper, A.F., Palin, J.M., Tulloch, A.J., Kula, J., Jongens, R., Spell, T.L., Pearson, N.J., 2009a. Tracking the influence of a continental margin on growth of a magmatic arc, Fiordland, New Zealand, using thermobarometry, thermochronology, and zircon U-Pb and Hf isotopes. Tectonics 28. https://doi.org/10.1029/2009TC002489 n/a-n/a.

Scott, J.M., Cooper, A.F., Tulloch, A.J., Spell, T.L., 2011. Crustal thickening of the early cretaceous paleo-pacific gondwana margin. Gondwana Res. 20, 380–394. https://doi.org/10.1016/j.gr.2010.10.008.

Scott, J.M., Palin, J.M., Cooper, A.F., King, R.P., 2009b. Polymetamorphism , zircon growth and retention of early assemblages through the dynamic evolution of a continental arc in Fiordland , New Zealand. J. Metamorph. Geol. 27, 281–294. https://doi.org/10.1111/j.1525-1314.2009.00817.x.

Stipp, M., Kunze, K., 2008. Dynamic recrystallization near the brittle-plastic transition in naturally and experimentally deformed quartz aggregates. Tectonophysics 448, 77–97. https://doi.org/10.1016/j.tecto.2007.11.041.

Stipp, M., Stünitz, H., Heilbronner, R., Schmid, S.M., 2002. The eastern Tonale fault zone: a “natural laboratory” for crystal plastic deformation of quartz over a temperature range from 250 to 700 °C. J. Struct. Geol. 24, 1861–1884. https://doi.org/10.1016/S0191-8141(02)00035-4.

Stipp, M., Tullis, J., 2003. The recrystallized grain size piezometer for quartz the recrystallized grain size piezometer for quartz. Geophys. Res. Lett. 30, 1–5. https://doi.org/10.1029/2003GL018444.

Stipp, M., Tullis, J., Scherwath, M., Behrmann, J.H., 2010. A new perspective on paleopiezometry: dynamically recrystallized grain size distributions indicate mechanism changes. Geology 38, 759–762. https://doi.org/10.1130/G31162.1.

Thomas, L.A., Wooster, W.A., 1951. Piezocrescence-the growth of dauphine twinning in quartz under stress. Proc. R. Soc. London A Math. Phys. Eng. Sci. 208, 43–62. https://doi.org/10.1098/rspa.1951.0143.

Toy, V.G., Prior, D.J., Norris, R.J., 2008. Quartz fabrics in the Alpine Fault mylonites: influence of pre-existing preferred orientations on fabric development during progressive uplift. J. Struct. Geol. 30, 602–621. https://doi.org/10.1016/j.jsg.2008.01.001.

Tullis, J., Christie, J.M., Griggs, D.T., 1973. Microstructures and preferred orientations of experimentally deformed quartzites. Geol. Soc. Am. Bull. 84, 297–314. https://doi.org/10.1130/0016-7606(1973)84<297:MAPOOE>2.0.CO;2.

Tullis, J., Tullis, T., 1972. Preferred orientation of quartz produced by mechanical Dauphiné twinning: thermodynamics and axial experiments. Flow facture rocks. Geophys. Monogr. 16, 67–82. https://doi.org/10.1029/GM016p0067.

Wenk, H.-R., Bortolotti, M., Barton, N., Oliver, E., Brown, D., 2007. Dauphine twinning and texture memory in polycrystalline quartz. Part 2 : in situ neutron diffraction compression experiments. Phys. Chem. Miner. 34, 599–607. https://doi.org/10.1007/s00269-007-0174-6.

Wenk, H.-R., Rybacki, E., Dresen, G., Lonardelli, I., Barton, N., Hermann, F., Gonzalez, G., 2006. Dauphine twinning and texture memory in polycrystalline quartz. Part 1 : experimental deformation of novaculite. Phys. Chem. Miner. 33, 667–676. https://doi.org/10.1007/s00269-006-0115-9.

Wenk, H., Barton, N., Bortolotti, M., Vogel, S.C., Voltolini, M., Lloyd, G.E., Gonzalez, G. B., 2009. Dauphine twinning and texture memory in polycrystalline quartz. Part 3: texture memory during phase transformation. Phys. Chem. Miner. 36, 567–583. https://doi.org/10.1007/s00269-009-0302-6.